

# Synthesis of Silicon Carbide Ceramic Composites with $\text{CeO}_2$ Powder



Luke R. Sadergaski  
Sarah Graham  
Jeremy Malmstead  
Andrew J. Miskowiec  
James W. Klett

**May 2022**

## DOCUMENT AVAILABILITY

Reports produced after January 1, 1996, are generally available free via US Department of Energy (DOE) SciTech Connect.

**Website** [www.osti.gov](http://www.osti.gov)

Reports produced before January 1, 1996, may be purchased by members of the public from the following source:

National Technical Information Service  
5285 Port Royal Road  
Springfield, VA 22161  
**Telephone** 703-605-6000 (1-800-553-6847)  
**TDD** 703-487-4639  
**Fax** 703-605-6900  
**E-mail** [info@ntis.gov](mailto:info@ntis.gov)  
**Website** <http://classic.ntis.gov/>

Reports are available to DOE employees, DOE contractors, Energy Technology Data Exchange representatives, and International Nuclear Information System representatives from the following source:

Office of Scientific and Technical Information  
PO Box 62  
Oak Ridge, TN 37831  
**Telephone** 865-576-8401  
**Fax** 865-576-5728  
**E-mail** [reports@osti.gov](mailto:reports@osti.gov)  
**Website** <http://www.osti.gov/>

This report was prepared as an account of work sponsored by an agency of the United States Government. Neither the United States Government nor any agency thereof, nor any of their employees, makes any warranty, express or implied, or assumes any legal liability or responsibility for the accuracy, completeness, or usefulness of any information, apparatus, product, or process disclosed, or represents that its use would not infringe privately owned rights. Reference herein to any specific commercial product, process, or service by trade name, trademark, manufacturer, or otherwise, does not necessarily constitute or imply its endorsement, recommendation, or favoring by the United States Government or any agency thereof. The views and opinions of authors expressed herein do not necessarily state or reflect those of the United States Government or any agency thereof.

Radioisotope Science and Technology Division

**Synthesis and Characterization of Silicon Carbide Ceramic Composites with CeO<sub>2</sub> Powder**

Luke R. Sadergaski  
Sarah Graham  
Jeremy Malmstead  
Andrew J. Miskowiec  
James W. Klett

May 2022

Prepared by  
OAK RIDGE NATIONAL LABORATORY  
Oak Ridge, TN 37831-6283  
managed by  
UT-BATTELLE, LLC  
for the  
US DEPARTMENT OF ENERGY  
under contract DE-AC05-00OR22725



# CONTENTS

LIST OF FIGURES .....	v
LIST OF TABLES .....	vi
ABBREVIATIONS .....	vii
ACKNOWLEDGMENTS .....	ix
ABSTRACT.....	1
1. BACKGROUND AND MOTIVATION .....	2
1.1 NUCLEAR WASTE .....	2
1.2 SILICON CARBIDE .....	2
1.3 MOTIVATION .....	3
2. MATERIALS AND METHODS.....	3
2.1 MATERIALS.....	3
2.2 SYNTHESIS .....	3
2.3 SEM-EDS SAMPLE PREPARATION AND ANALYSIS .....	5
2.4 ADDITIONAL CHARACTERIZATION .....	6
3. RESULTS AND DISCUSSION .....	6
3.1 POWDER X-RAY DIFFRACTION.....	6
3.2 RAMAN SPECTROSCOPY .....	12
3.3 OPTICAL IMAGES .....	17
3.4 SEM-EDS ANALYSIS.....	21
3.4.1 SEM and BSE Images.....	21
3.4.2 EDS Maps .....	23
3.5 DENSITY MEASUREMENTS.....	25
4. SUMMARY AND MAJOR CONCLUSIONS.....	26
4.1 FUTURE STUDIES AND APPLICATIONS.....	26
4.2 CONCLUSIONS.....	26
REFERENCES .....	27



## LIST OF FIGURES

Figure 2.1. SMP-10 and CeO <sub>2</sub> powder slurry in a 3D printed crucible (left) and CeO <sub>2</sub> containing a SiC sample after curing and pyrolysis (right). .....	4
Figure 2.2. Samples submerged in SMP-10 resin while pulling a vacuum. ....	5
Figure 2.3. Example SiC-CeO <sub>2</sub> containing samples cut and polished in epoxy and wrapped in Cu tape.....	6
Figure 3.1. pXRD for R1 samples 1–3.....	7
Figure 3.2. pXRDs for R2 samples 1–3.....	7
Figure 3.3. pXRDs for R3 samples 1–3.....	8
Figure 3.4. pXRDs for R4 samples 1–3.....	8
Figure 3.5. pXRDs for R5 samples 1–3.....	9
Figure 3.6. Powder x-ray diffractogram for sample R2_1 (labeled R2 S2 in color key) compared with reported diffraction data (PDF: 00-0004-0593).....	9
Figure 3.7. Powder x-ray diffractogram for R1 after decomposition at 2,100 °C. ....	10
Figure 3.8. Unprocessed powder x-ray diffractograms for Rs 2–5 after decomposition at 2,100 °C.....	11
Figure 3.9. Raman spectrum of CeO <sub>2</sub> powder with Voigt fit (R <sup>2</sup> 0.9967). ....	12
Figure 3.10. Raman map with empty modelling component 1 (blue) compared to a spectrum (red) for sample R4_3 (recipe 4). ....	13
Figure 3.11. Raman map with principal component 1 (blue) compared to a spectrum (red).....	14
Figure 3.12. Example spectra (10) taken from the first scan in the map shown in Figure 3.9.....	14
Figure 3.13. Linear regression of peak position vs. FWHM for spectra shown in Figure 3.09.....	15
Figure 3.14. Raman map with empty modelling component 1 (blue) compared to a spectrum (red) for R2_3. ....	16
Figure 3.15. Raman map with empty modelling component 1 (blue) compared to a spectrum (red) for R3_3. ....	16
Figure 3.16. Raman map with empty modelling component 1 (blue) compared to a spectrum (red) for R5_S3. Note dark region corresponding to carbon fiber.....	17
Figure 3.17. Optical image for sample R1_3 using the 20× objective.....	18
Figure 3.18. Optical image for sample R2_3 using the 20× objective.....	18
Figure 3.19. Optical image for sample R3_3 using the 20× objective.....	19
Figure 3.20. Optical image for sample R4_3 using the 20× objective.....	19
Figure 3.21. Optical image for sample R5_3 using the 20× objective.....	20
Figure 3.22. Optical image for sample R5_3 using the 100× objective.....	20
Figure 3.23. SEM image (left) in BSE mode (right) for R1. Bright particles (<1 μm) correspond to high-Z material (i.e., Ce oxides). ....	21
Figure 3.24. SEM image (left) in BSE mode (right) for R2. Bright particles (<1 μm) correspond to high-Z material (i.e., Ce oxides). ....	21
Figure 3.25. SEM image (left) in BSE mode (right) for R3. Bright particles (<1 μm) correspond to high-Z material (i.e., Ce oxides). ....	22
Figure 3.26. SEM image (left) in BSE mode (right) for R4. Bright particles (<1 μm) correspond to high-Z material (i.e., Ce oxides). ....	22
Figure 3.27. SEM image (left) in BSE mode (right) for R5. Bright particles (<1 μm) correspond to high-Z material (i.e., Ce oxides). ....	22
Figure 3.28. SEM image (left) and BSE elemental map (right) for R1. EDS results indicate that bright regions likely correspond to Ce oxide particles. Note the 5 μm scale bar. ....	23
Figure 3.29. SEM image (left) and BSE elemental map (right) for R2. EDS results indicate that bright regions likely correspond to Ce oxide particles. Note the 5 μm scale bar. ....	23
Figure 3.30. SEM image (left) and BSE elemental map (right) for R3. EDS results indicate that bright regions likely correspond to Ce oxide particles. Note the 200 μm scale bar. ....	24

Figure 3.31. SEM image (left) and BSE elemental map (right) for R3. EDS results indicate that bright regions likely correspond to Ce oxide particles. Note the 5  $\mu\text{m}$  scale bar. .... 24

Figure 3.32. SEM image (left) and BSE elemental map (right) for R4. EDS results indicate that bright regions likely correspond to Ce oxide particles. Note the 5  $\mu\text{m}$  scale bar. .... 24

Figure 3.33. SEM image (left) and BSE elemental map (right) for R5. EDS results indicate that bright regions likely correspond to Ce oxide particles. Note the 20  $\mu\text{m}$  scale bar. .... 25

**LIST OF TABLES**

Table 2.1. Synthetic mixtures ..... 4

Table 3.1. Sample density profiles..... 25

## ABBREVIATIONS

ABS	acrylonitrile butadiene styrene
BSE	backscatter electron
CVD	chemical vapor deposition
EDS	energy-dispersive x-ray spectroscopy
FWHM	full width at half maximum
ICSD	Inorganic Crystal Structure Database
ORNL	Oak Ridge National Laboratory
PCA	principal component analysis
PDC	polymer-derived ceramic
PDF	powder diffraction file
PIP	polymer infiltration and pyrolysis
pXRD	powder x-ray diffraction
SEM	scanning electron microscopy
SiC	silicon carbide
STD	standard deviation
XRD	x-ray diffraction



## **ACKNOWLEDGMENTS**

The author's wish to thank Kristian G. Myhre for helpful discussions regarding the scope of this work and Chris Gilbert for help with pyrolysis. Funding for this work was provided by the National Nuclear Security Administration. This work used resources at the Manufacturing Demonstration Facility operated by Oak Ridge National Laboratory.



## ABSTRACT

This study pioneers the fabrication and characterization of silicon carbide (SiC) containing cerium dioxide ( $\text{CeO}_2$ ).  $\text{CeO}_2$  powder was tested as a surrogate for actinide oxide waste forms such as uranium dioxide ( $\text{UO}_2$ ) and plutonium dioxide ( $\text{PuO}_2$ ). Several syntheses were evaluated with varying amounts of preceramic polymer (SMP-10 resin) and  $\text{CeO}_2$  containing either SiC fiber, carbon fiber, or no fibers. Scanning electron microscopy (SEM) was used to characterize morphology and compositional differences, and energy-dispersive x-ray spectroscopy (EDS) was used to provide semiquantitative elemental analysis. In addition, each sample was characterized by density, powder x-ray diffraction (pXRD), and Raman spectroscopy. Samples containing nearly more than four times  $\text{CeO}_2$  powder than SMP-10 resin by mass had the best properties. This research establishes a unique synthesis for SiC containing high concentrations of  $\text{CeO}_2$  powder to illustrate how it may be managed as a potential waste form.

# 1. BACKGROUND AND MOTIVATION

## 1.1 NUCLEAR WASTE

Identifying a permanent storage solution for high-level and transuranic nuclear waste is one of the most pressing challenges of the 21<sup>st</sup> century. At this time, no universal methods have been established for disposing of used nuclear fuel from commercial nuclear reactors or high-level waste from nuclear weapons production. The Blue Ribbon Commission on America's Nuclear Future determined that the best way to dispose of nuclear waste is in underground geologic repositories.<sup>1</sup> These repositories are being specially designed to maintain their integrity for millions of years, with natural and engineered barriers to limit the mobility of radionuclides in the biosphere. Barriers will include local geology and geochemistry, engineered storage containers (e.g., metal/cement), and clay backfill.<sup>2</sup> Because the proposed storage containers will likely be breached before all the radionuclides have decayed away, a secondary engineered barrier made up of the clay minerals is being considered for US repositories: the clay effectively limits water flux towards waste containers, is relatively abundant, and serves as an effective sorbent material for numerous contaminants. However, there is still a need for research and development to improve the robustness and longevity of such storage facilities.

It is important to continue developing effective, efficient storage vessels for high-level and transuranic nuclear waste. Novel materials have the potential to enhance storage properties and improve performance assessment models and may significantly advance the immense work that will be required to site, license, construct, and operate a permanent disposal facility. Actinides such as <sup>239</sup>Pu, <sup>237</sup>Np, and <sup>238</sup>U are long-lived and have a major impact on long-term risk assessments for geologic repositories. Materials which can effectively secure these actinides and other radionuclides generated from the nuclear fuel cycle and dismantled nuclear weapons must be developed.

## 1.2 SILICON CARBIDE

Silicon carbide (SiC) is a hard chemical compound that occurs in nature as the extremely rare mineral moissanite. Although it is rare on Earth, it is a common form of stardust found near carbon-rich stars. The thermodynamically stable solid phases present in general Si-O-C systems include SiC, SiO<sub>2</sub>, Si, and C, with gaseous phases of O, CO, CO<sub>2</sub>, and SiO. The formation of a SiO<sub>x</sub>C<sub>y</sub> glassy phase is known to occur during preceramic polymer-derived SiC processing.

SiC has been mass produced in powder or crystal form for more than a century for use in various applications, including use as an abrasive polishing material, in semiconductor electronic devices, for thin filament pyrometry, and for applications requiring high endurance such as car brakes and ceramic plates in bullet-proof vests. SiC is relatively lightweight (density ~3 g·cm<sup>-3</sup>) and is chemically inert. It cannot be corroded by any acids, molten salts, or alkalis, even up to temperatures near 800 °C. It is also resistant to oxidation and has a low coefficient of thermal expansion, even when exposed to extreme temperatures.

SiC exists in nearly 250 crystalline forms, with the most common polymorph being alpha silicon carbide ( $\alpha$ -SiC).<sup>3,4</sup> The process of sintering binds grains of SiC together to form strong ceramics, and composite materials can be formed when SiC fibers are added to the polymer matrix. Adding ceramic fibers to the matrix improves fracture performance when used in monolith form. Several synthesis methods are available to produce SiC. The simplest process is to heat silica sand and carbon in an Acheson furnace at high temperature (~1,600 °C). Other methods include the Lely process, chemical vapor deposition (CVD), and pyrolysis of preceramic polymers. Pyrolysis is advantageous because it can be used to form various shapes before the ceramic is generated.

The preceramic polymer SMP-10 by Starfire Systems, Inc., is the only commercially available one-component liquid precursor to SiC ceramics. It can be used to manufacture SiC ceramic matrix composites, monolithic parts created from ceramic powders, high-temperature SiC coatings, and joined SiC materials. Polymer derived ceramics (PDCs) are synthesized by pyrolysis of preceramic polymers under an inert atmosphere at relatively low temperature. SMP-10 resin is relatively easy to use, and it can produce high-purity ceramic yields of near stoichiometric SiC while reducing manufacturing cycle times.

### 1.3 MOTIVATION

Many of SiC's chemical and thermal properties could make it a robust, flexible engineered barrier for nuclear waste storage. Exploratory experiments are needed to assess the feasibility of SiC as an appropriate waste form for nuclear materials in powder form. Si and C atoms form strong tetrahedral covalent bonds in a SiC crystal with an energy of 4.6 eV. Numerous storage vessel forms are conceivable. The primary focus of this report is to describe the novel synthesis of a SiC cermet that contains CeO<sub>2</sub> powder in the composite material. Ce(IV) oxide, which adopts the fluorite crystal structure (space group Fm $\bar{3}$ m), was used as a surrogate for U(IV) and Pu(IV) oxides. This report also explores whether CeO<sub>2</sub> powder could replace ceramic fibers while maintaining acceptable composite properties. Replacing SiC<sub>f</sub> with oxide could simplify the process and may make it more cost effective. Fibers are typically used to minimize cracking in the first and second polymer infiltration and pyrolysis (PIP) cycles.

Several combinations of SMP-10, CeO<sub>2</sub>, SiC fiber, and carbon fiber were used to synthesize SiC composites that homogeneously encapsulated the CeO<sub>2</sub> powder. These parameters were explored to determine the optimal loading of CeO<sub>2</sub> powder and to discern whether CeO<sub>2</sub> powder could replace commonly used fiber materials while maintaining sample characteristics. The samples were characterized using scanning electron microscopy (SEM) and energy-dispersive x-ray spectroscopy (EDS), density, powder x-ray diffraction (pXRD), and Raman spectroscopy.

## 2. MATERIALS AND METHODS

### 2.1 MATERIALS

Chemicals were commercially obtained (American Chemical Society grade). SMP-10 resin was purchased from Starfires Systems Inc., and CeO<sub>2</sub> powder (<5  $\mu$ m, 99.9 % trace metals basis) was purchased from Sigma-Aldrich.

### 2.2 SYNTHESIS

SMP-10 resin, CeO<sub>2</sub> powder, SiC fiber (SiC<sub>f</sub>) and carbon fiber (C<sub>f</sub>) were mixed in various proportions as shown in Table 2.1. Four samples for each recipe were synthesized. The slurry was mixed to make a white paste before undergoing curing and pyrolysis. CeO<sub>2</sub> powder was mixed with SMP-10 at 1–2-gram increments; mixing was performed thoroughly by hand between each addition. After approximately half of the CeO<sub>2</sub> was added, either SiC<sub>f</sub> or C<sub>f</sub> was added and mixed by hand. Additional CeO<sub>2</sub> was added until the desired consistency was achieved. The lower concentration mixtures (recipe 1 [R1] and recipe 3 [R3]) were relatively free flowing, whereas the higher concentration mixtures (R2, R4, and R5) became a non-Newtonian fluid.

The synthesis followed multiple two-step cure and pyrolysis cycles. The mixtures were placed in 3D printed crucibles made from acrylonitrile butadiene styrene (ABS) plastic and were heat treated at 250 °C for two hours at a slow rate to avoid spalling or splitting caused by the pressure of trapped gases (Figure 2.1, left). The low temperature-cured polymer is a cross-linked carbosilane resin. Next, each sample was

pyrolyzed at 850 °C in an inert atmosphere to generate SiC parts (Figure 2.1, right). The 3D printed crucible allowed the samples (i.e., parts) to take shape during curing, but it was removed by high temperature during pyrolysis.

**Table 2.1. Synthetic mixtures**

Recipe	SMP-10 (g)	CeO <sub>2</sub> (g)	SiC <sub>f</sub> (g)	C <sub>f</sub> (g)	wt% CeO <sub>2</sub>
1	7.18	16.02	0.724	0	0.67
2	4.30	19.23	0.719	0	0.79
3	7.22	16.07	0	0	0.69
4	4.33	19.39	0	0	0.82
5	4.29	19.33	0	0.740	0.79



**Figure 2.1. SMP-10 and CeO<sub>2</sub> powder slurry in a 3D printed crucible (left) and CeO<sub>2</sub> containing a SiC sample after curing and pyrolysis (right).**

Four PIP cycles were completed after the initial synthesis to minimize closed porosity. After each cycle, one sample from each recipe was characterized to determine if the process enhanced specimen characteristics. Infiltration cycles were completed in a fume hood. The process was to submerge samples in SMP-10 resin and pull a vacuum until no bubbles were observed (Figure 2.2). After infiltration, each sample was cured and pyrolyzed. One cycle included (1) infiltration by SMP-10 under vacuum, (2) curing at 250 °C, and (3) pyrolysis at 850 °C. Between cycles, specimens were gently cleaned of debris using sandpaper. The fourth sample from each recipe was heated up to 1,500 °C under nitrogen and then was heated under argon from 1,500–2,100 °C to carbonize the material.



**Figure 2.2. Samples submerged in SMP-10 resin while pulling a vacuum.**

### **2.3 SEM-EDS SAMPLE PREPARATION AND ANALYSIS**

The samples were prepared first using traditional metallographic processes. The samples were sectioned with a diamond wafering blade, mounted in epoxy, and then polished to a resolution of  $0.05\ \mu\text{m}$  using diamond abrasive and colloidal silica. Once polished, the samples were taped with copper, carbon-coated with 3 nm of graphite, and then ion-milled (6.0kV acc, 1.5kV dis) for 45 minutes at a  $10^\circ$  angle to the beam using the Hitachi ArBlade 5000 to reduce charging during microscopy and to prevent drifting (Figure 2.3)

SEM images were taken with a ZEISS Gemini 450 (a field emission SEM) at an accelerating voltage of 5kV. The secondary electron mode was used on two representative locations for each sample; imaging and elemental mapping were performed at both low- (150 $\times$ ) and high-resolutions (1,500 $\times$ ) at each location.



**Figure 2.3.** Example SiC-CeO<sub>2</sub> containing samples cut and polished in epoxy and wrapped in Cu tape.

## 2.4 ADDITIONAL CHARACTERIZATION

The balance of unmounted material for each sample was gently cleaned of debris after sectioning, air dried, and tested for bulk density using an AccuPyc II 1340 helium pycnometer. The prepared samples were imaged at a range of low and high magnifications (5–100×) on a Leica DM4000 optical microscope to identify regions of interest.

Samples were prepared for pXRD by grinding ~20 mg of the prepared material loading on a zero-background silicon substrate. Data were collected with a Proto AXRD benchtop powder diffractometer in Bragg–Brentano configuration with a Cu–K $\alpha$  ( $\lambda = 1.5406 \text{ \AA}$ ) x-ray source and a Dectris Mythen 1 K 1D detector. Axial divergence was reduced using incident and diffracted beam Soller slits and a 0.6 mm divergence slit. Data were collected in the range of 8–80° 2 $\theta$ , with a step velocity of 0.02° 2 $\theta$ /min. Raman point spectra and spectral maps were collected using a Renishaw inViaTM micro-Raman spectrometer. An excitation wavelength of 532 nm was used to collect data in the range of 100–1,250 cm<sup>-1</sup>, in combination with a 2,400 l/mm diffraction grating, with a resolution near ~1 cm<sup>-1</sup>. Depending on the sample, integration times varied from 1–10 s, and laser power settings varied from 5–100%.

## 3. RESULTS AND DISCUSSION

### 3.1 POWDER X-RAY DIFFRACTION

CeO<sub>2</sub> was identified in each specimen (Figure 3.1 through Figure 3.6) prior to high-temperature heating (Figure 3.7) based on pXRD results. Diffraction data obtained for CeO<sub>2</sub> in this work agreed with diffractograms reported in the Inorganic Crystal Structure Database (ICSD) (e.g., powder diffraction file [PDF] Card# 00–004–0593). An example comparison is shown in Figure 3.7. Other peaks corresponded to secondary Ce-based peaks such as Ce<sub>2</sub>O<sub>3</sub>, Ce<sub>7</sub>O<sub>12</sub>, CeO, Ce<sub>3</sub>O<sub>5</sub>, and other minor phases. The minor phases are more abundant in samples that contain less CeO<sub>2</sub> (R1 and R3).

SiC is known to occur in over 100 polytypes because of complicated nucleation and crystallization properties.<sup>3</sup> No obvious SiC phases were identified in the diffraction patterns, which is consistent with the synthesis conditions generally used to generate amorphous SiC samples. Pyrolysis to 850 °C forms glassy (amorphous) SiC.  $\beta$ -SiC tends to form at temperatures ranging from 1,500–1,600 °C and is characterized by doublet diffraction peaks near 35–37 2-Theta.

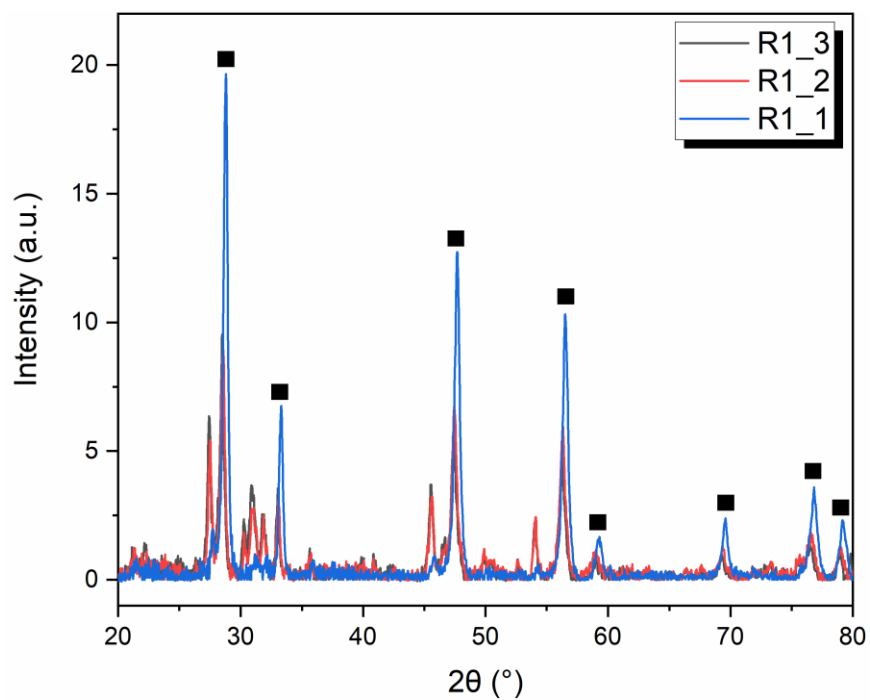


**Figure 3.1.** pXRD for R1 samples 1–3.  $\text{CeO}_2$  Bragg peaks are denoted by black squares.

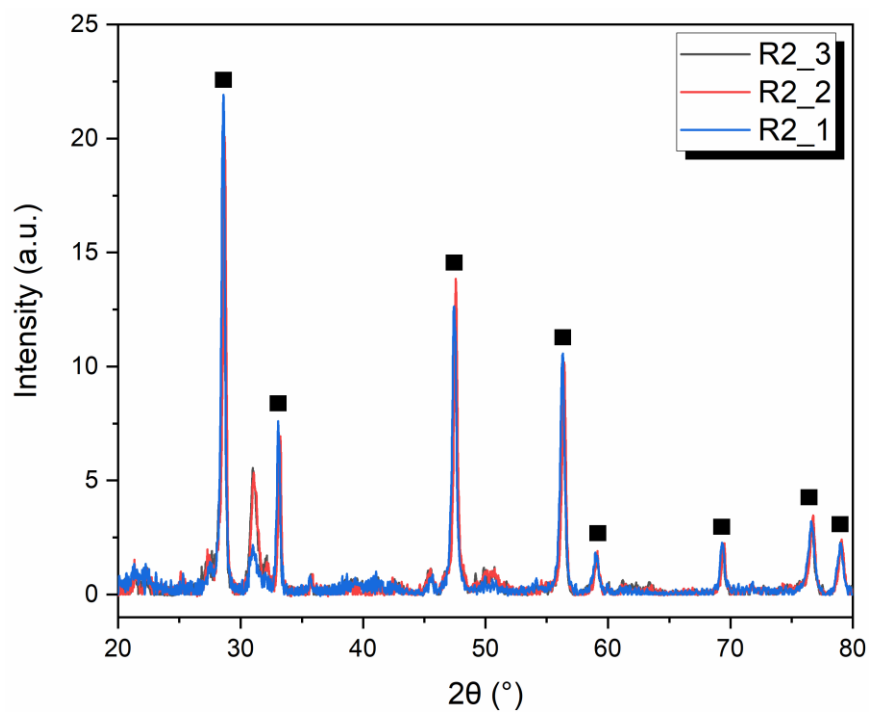


**Figure 3.2.** pXRDs for R2 samples 1–3.  $\text{CeO}_2$  Bragg peaks are denoted by black squares.

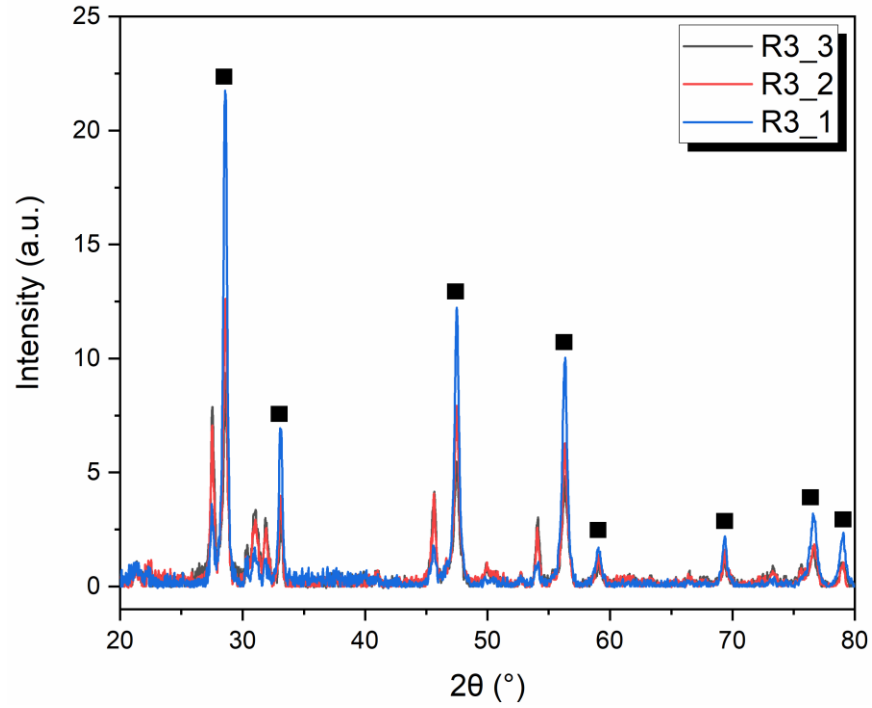


**Figure 3.3.** pXRDs for R3 samples 1–3.  $\text{CeO}_2$  Bragg peaks are denoted by black squares.

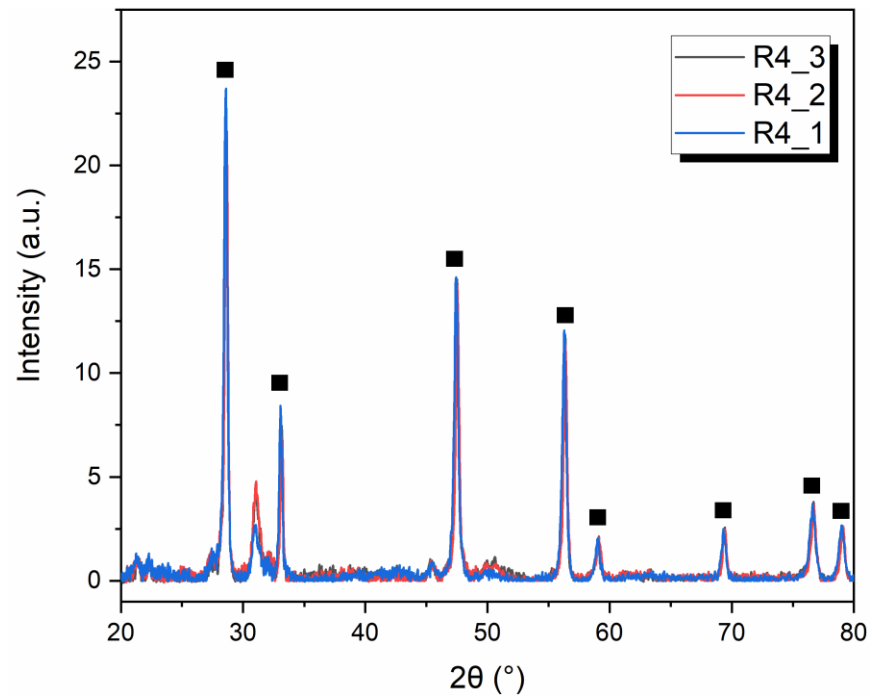


**Figure 3.4.** pXRDs for R4 samples 1–3.  $\text{CeO}_2$  Bragg peaks are denoted by black squares.

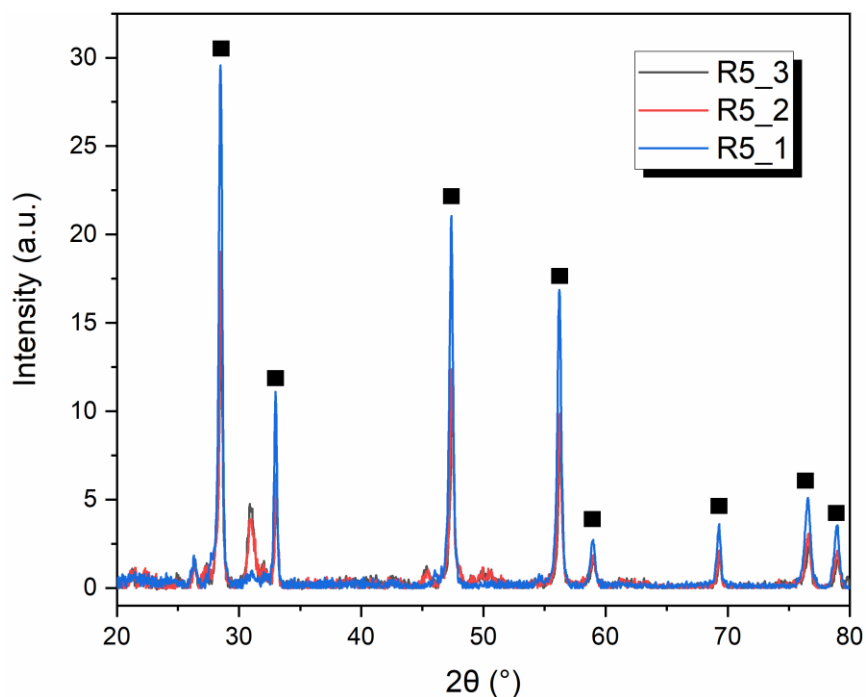


**Figure 3.5.** pXRDs for R5 samples 1–3. CeO<sub>2</sub> Bragg peaks are denoted by black squares.

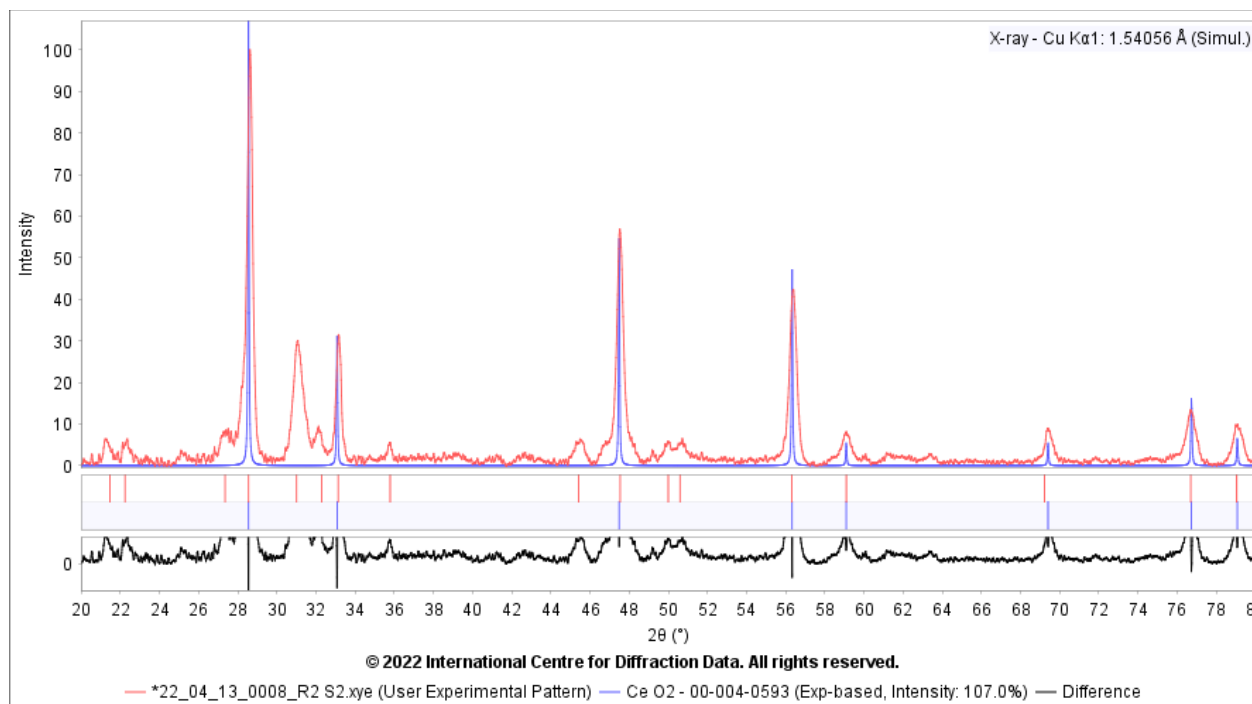


**Figure 3.6.** Powder x-ray diffractogram for sample R2\_1 (labeled R2 S2 in color key) compared with reported diffraction data (PDF: 00-0004-0593).

Powder diffraction patterns changed significantly after heat treatment to 2,100 °C (see Figure 3.7). CeO<sub>2</sub> was not identified in this diffractogram. Both sharp and broad peaks indicated the presence of at least one or more crystalline phases and an amorphous phase. Unprocessed diffractograms for the other recipes are shown in Figure 3.8. When the samples were initially removed from the inert furnace, they retained their shapes for a few seconds until they decomposed to powder form, likely after reacting with moisture in the ambient air. Powders were dark green in color. This finding was unexpected because the melting point of CeO<sub>2</sub> is 2,400 °C, and the upper limit of stability for SiC is approximately 2,500 °C. One possible explanation is that a eutectic formed, causing a lower melting point for the mixture.

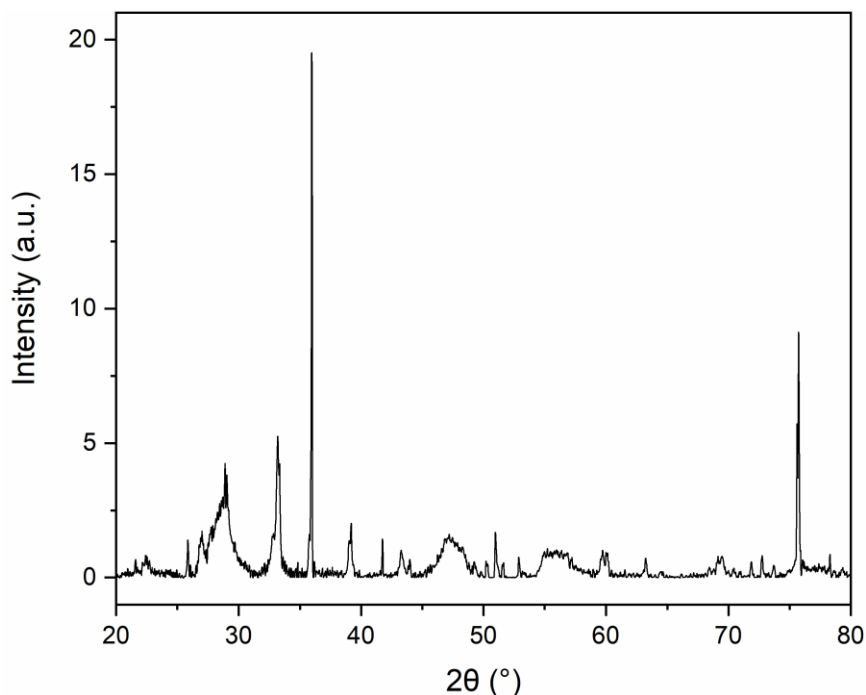


**Figure 3.7. Powder x-ray diffractogram for R1 after decomposition at 2,100 °C.**

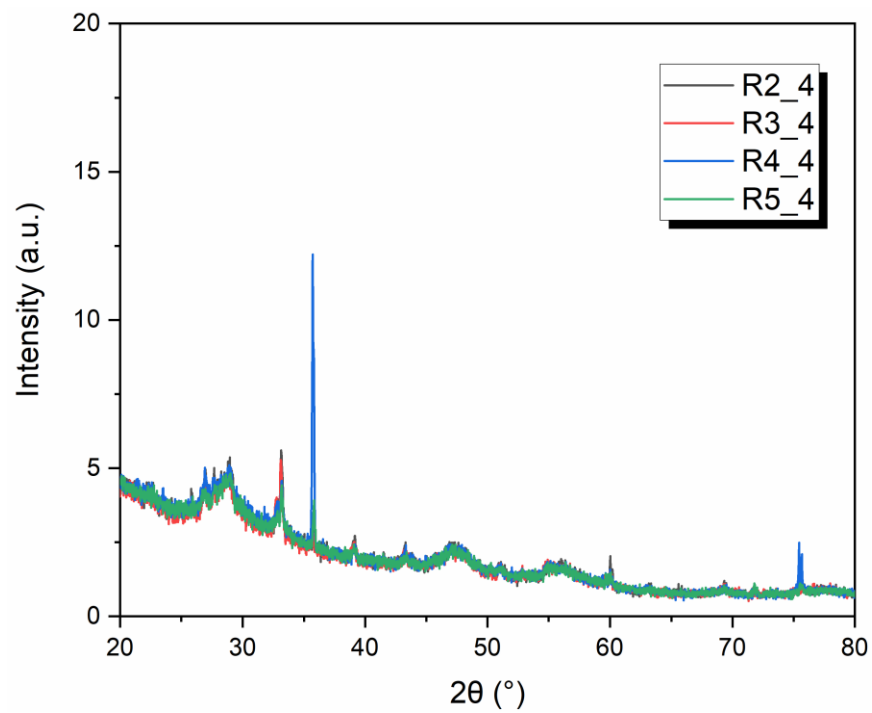


**Figure 3.8. Unprocessed powder x-ray diffractograms for Rs 2–5 after decomposition at 2,100 °C.**

### 3.2 RAMAN SPECTROSCOPY

The Raman spectrum of CeO<sub>2</sub> is straightforward, comprising a single sharp Raman active peak centered near 465 cm<sup>-1</sup> (T<sub>2g</sub> symmetry) in the Raman fingerprint region.<sup>5</sup> Voigt peak fitting using OriginPro data analysis and graphing software indicated that the peak comprises one vibrational band at 465 cm<sup>-1</sup> with a full width at half maximum (FWHM) of 8.1 cm<sup>-1</sup> (Figure 3.9) Raman maps were taken of the mounted and polished samples to measure the distribution of CeO<sub>2</sub> particles on the surface.

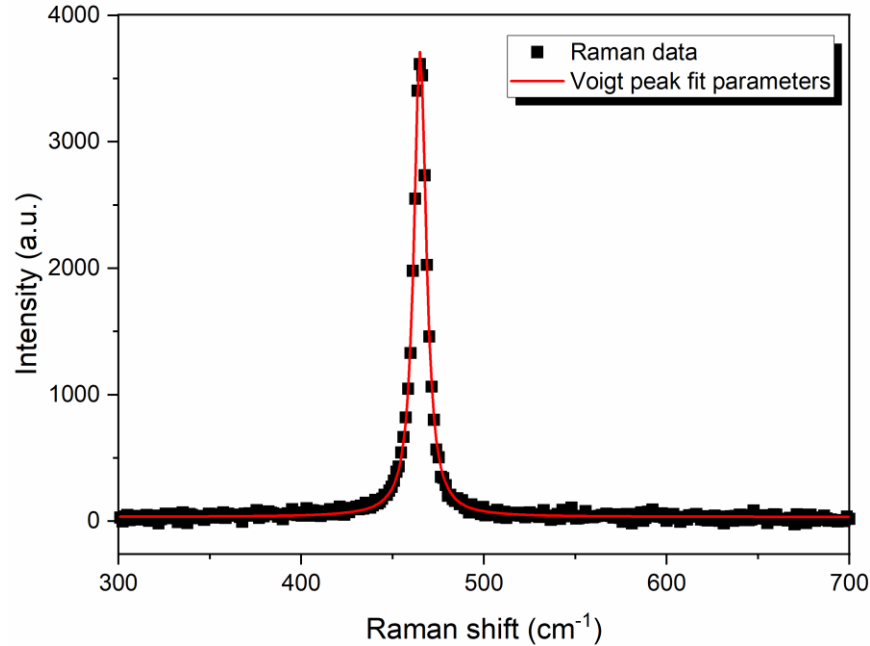


**Figure 3.9. Raman spectrum of CeO<sub>2</sub> powder with Voigt fit (R<sup>2</sup> 0.9967).**

Raman maps were taken on 200- and 20-micron length scales with the 5× and 50× objectives, respectively. The 50× objective was particularly useful for identifying species in regions that appeared to be relatively homogenous. The SiC composite did not appear to be Raman active, but CeO<sub>2</sub>-related components were Raman active, and 2D correlation maps were highly informative. This technique is preferred over EDS mapping because it not only provides elemental compositions, but also the distribution of chemical fingerprints. However, this can only be applied for Raman active species.

*Empty modelling* is Renishaw’s chemometric method for extracting spectral components from Raman data. It can indicate the locations of specific chemical species in 2D maps based on Raman fingerprints. Empty modeling is useful for determining what is present in the sample, where it is, and its dimensions. This method determines which spectra are key components and generates images depicting their distribution on the sample’s surface. Empty modelling results are typically easier to interpret than more those from abstract techniques such as principal component analysis (PCA).

An example empty modeling 2D correlation map is shown in Figure 3.10 for sample R4\_3 (R4 after three PIP cycles). Figure 3.11 includes a PCA map for comparison. Additional components did not appear to represent significant spectral features (data are not shown here). The analysis revealed two distinct CeO<sub>2</sub> species: one with a less intense, broad T<sub>2g</sub> band, and another with a more intense, sharper T<sub>2g</sub> band (Figure 3.12) The broad and low intensity peaks correspond to regions where the CeO<sub>2</sub> is incorporated in the composite matrix, whereas the sharper peaks (bright regions) correspond to non-incorporated CeO<sub>2</sub> particles.

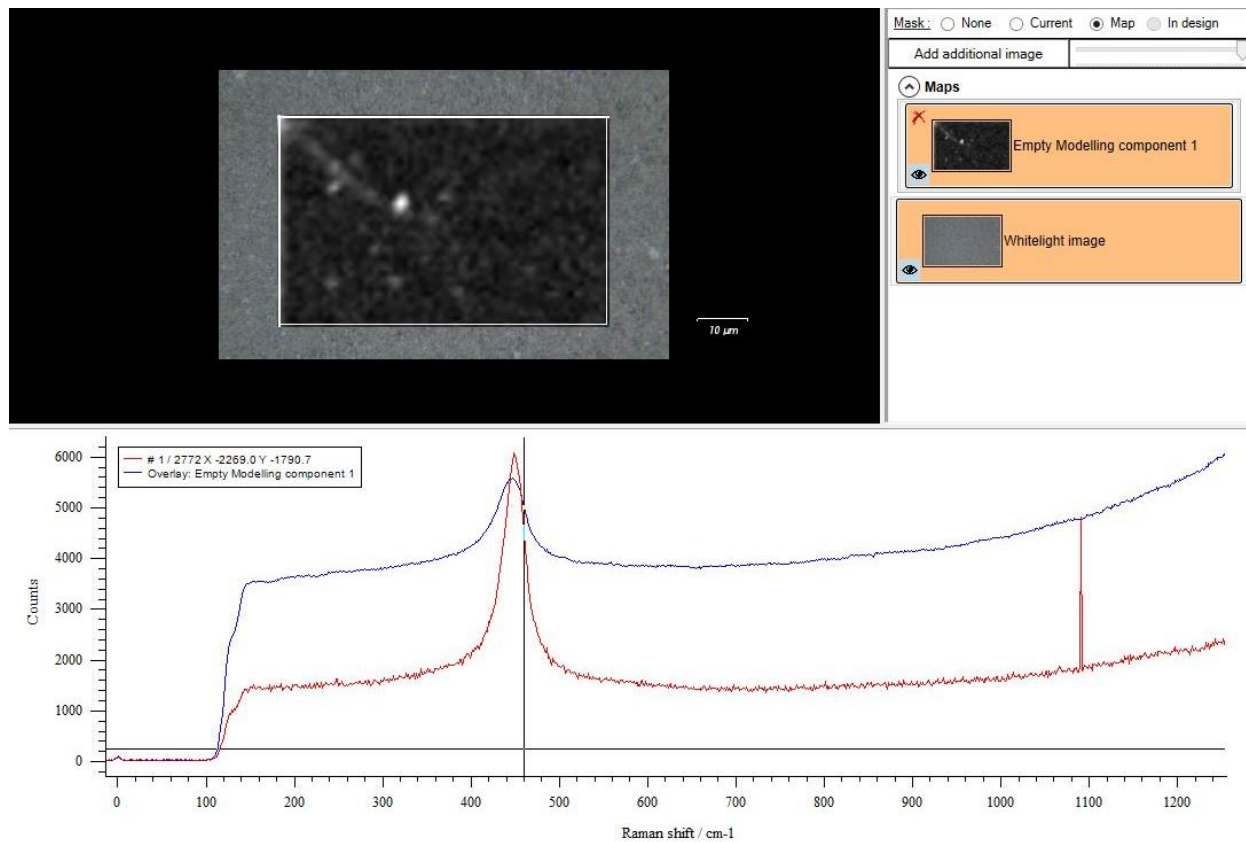


**Figure 3.10. Raman map with empty modelling component 1 (blue) compared to a spectrum (red) for sample R4\_3 (recipe 4). Raman peak near 450 cm<sup>-1</sup> corresponds to CeO<sub>2</sub>. Sample not homogenous on microscale (note varying peak intensity on map).**

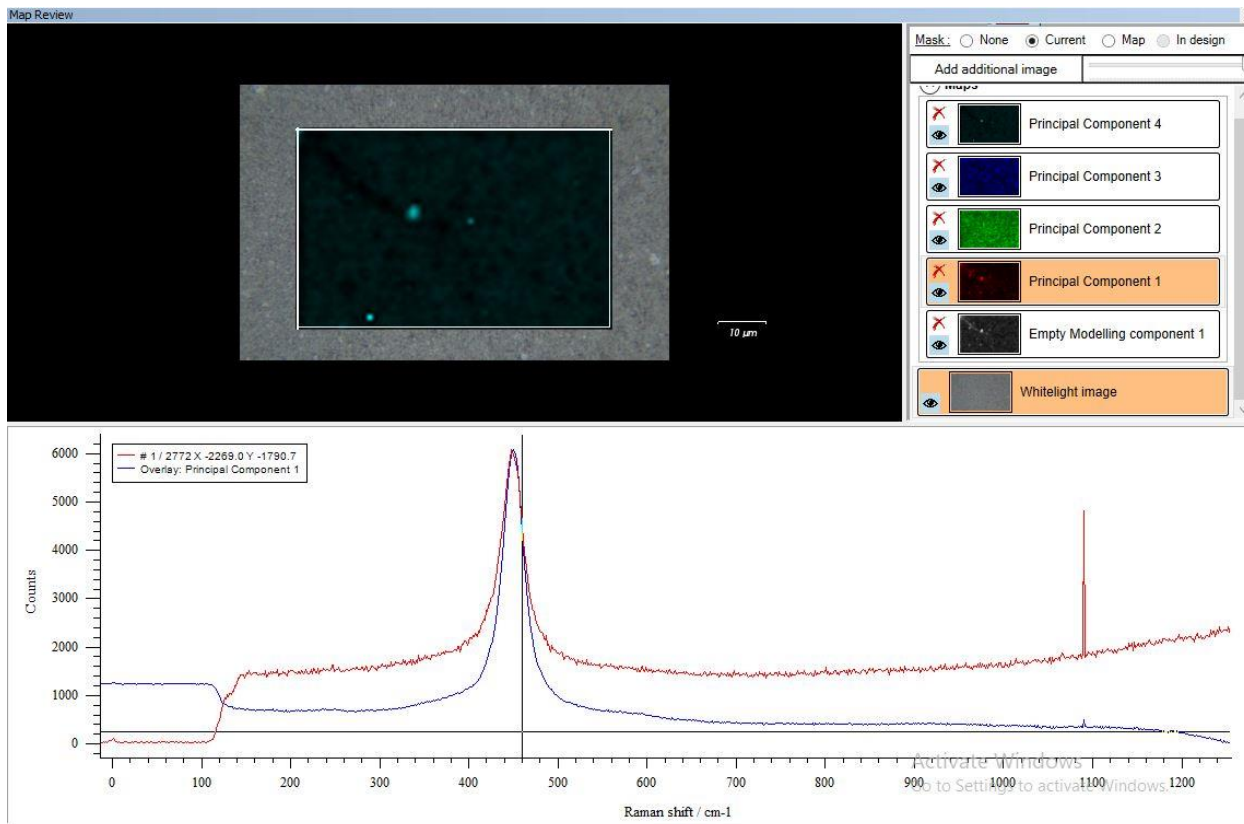


**Figure 3.11. Raman map with principal component 1 (blue) compared to a spectrum (red).** Raman peak near  $450\text{ cm}^{-1}$  corresponds to  $\text{CeO}_2$ . Sample is not homogenous on the microscale (note varying peak intensity on map).

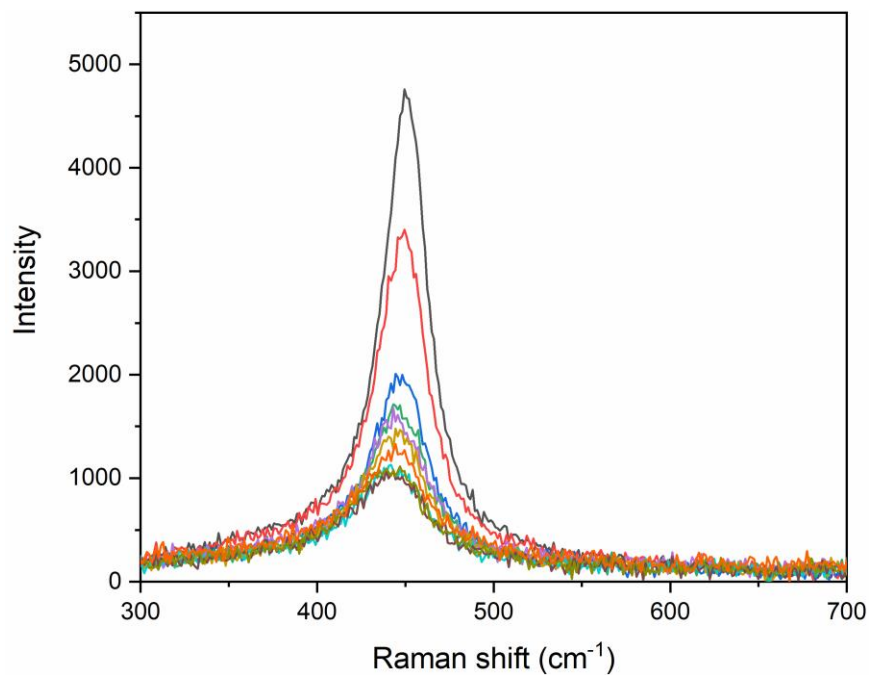


**Figure 3.12. Example spectra (10) taken from the first scan in the map shown in Figure 3.9.** Note changes in  $\text{CeO}_2$   $T_{2g}$  band peak intensity and FWHM.

With decreasing Raman wavenumber ( $\text{cm}^{-1}$ ) or lower energy, the FWHM increased (Figure 3.13). The FWHM of surface agglomerates had narrower FWHM values, whereas particles that were more homogeneously dispersed in the sample had much larger FWHM values. In any case, the FWHM was broader than the control ( $8.1 \text{ cm}^{-1}$ ). FWHM reflects the structural distribution of Raman active materials. Sharper Raman peaks generally correspond to more crystalline materials, and broader peaks correspond to amorphous materials. The vibrational frequency or peak position is influenced by intramolecular and intermolecular force constants. A shift in peak position indicates that the packing of the molecules in the crystal lattice changed upon pyrolysis and at various levels of incorporation in the SiC matrix.

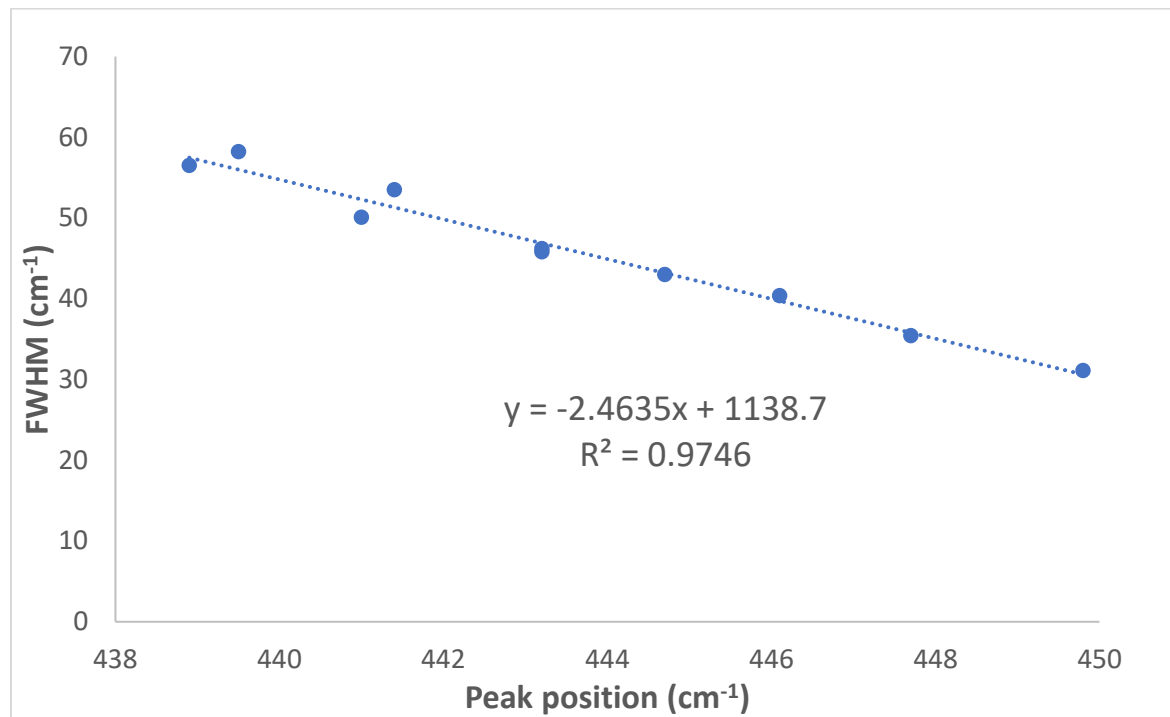


**Figure 3.13. Linear regression of peak position vs. FWHM for spectra shown in Figure 3.09.**

The optical images of R2 samples show white particulates, but Raman maps reveal that these particles were not  $\text{CeO}_2$  (Figure 3.13). Support spot spectra were also acquired, but the data are not shown here. The peak intensity of  $\text{CeO}_2$  species was not as intense and sharp in comparison to R4 data (compare Figure 3.13 to Figure 3.10). This suggests that  $\text{SiC}_f$  improved the sample properties. Fewer  $\text{CeO}_2$  particles were identified on the surface of R3 samples (Figure 3.14) than on R4 sample surfaces (Figure 3.10). This indicates that loading less material improves incorporation of  $\text{CeO}_2$  into the composite matrix on the microscale. However, it does not necessary improve other characteristics such as tensile strength.

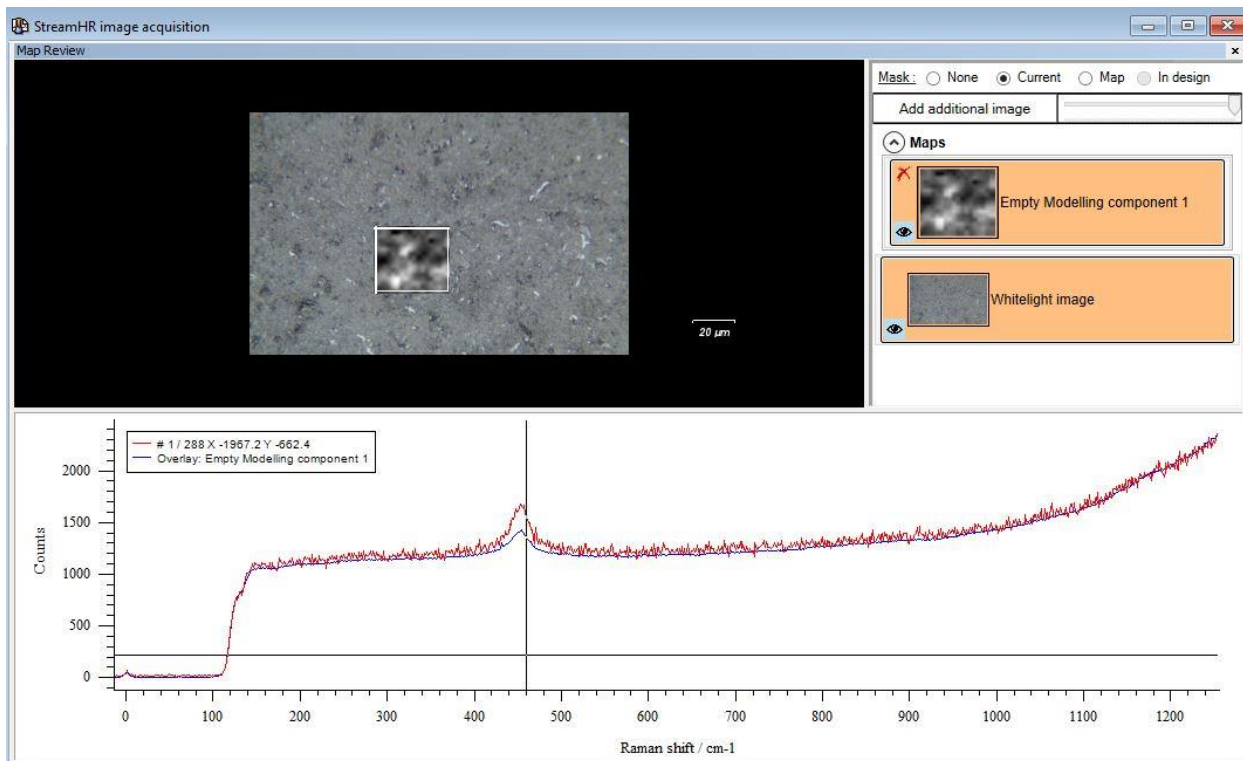


Figure 3.14. Raman map with empty modelling component 1 (blue) compared to a spectrum (red) for R2\_3.

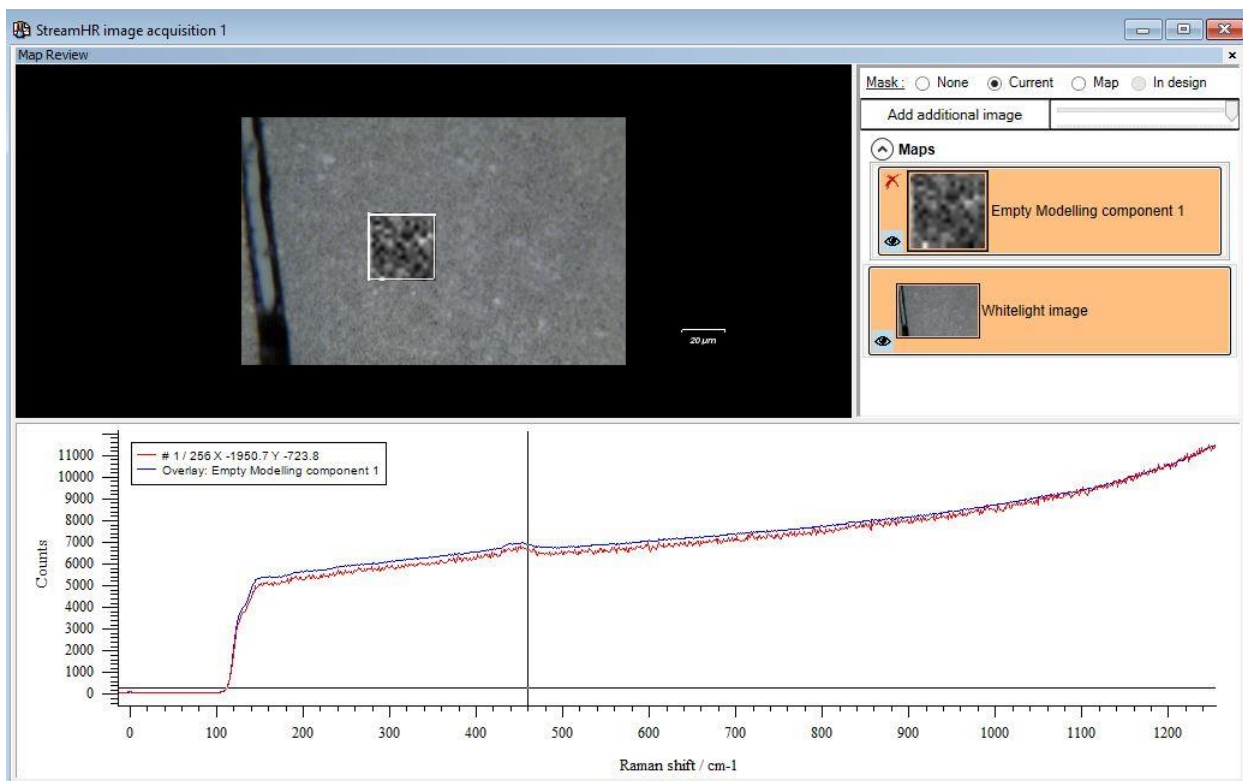
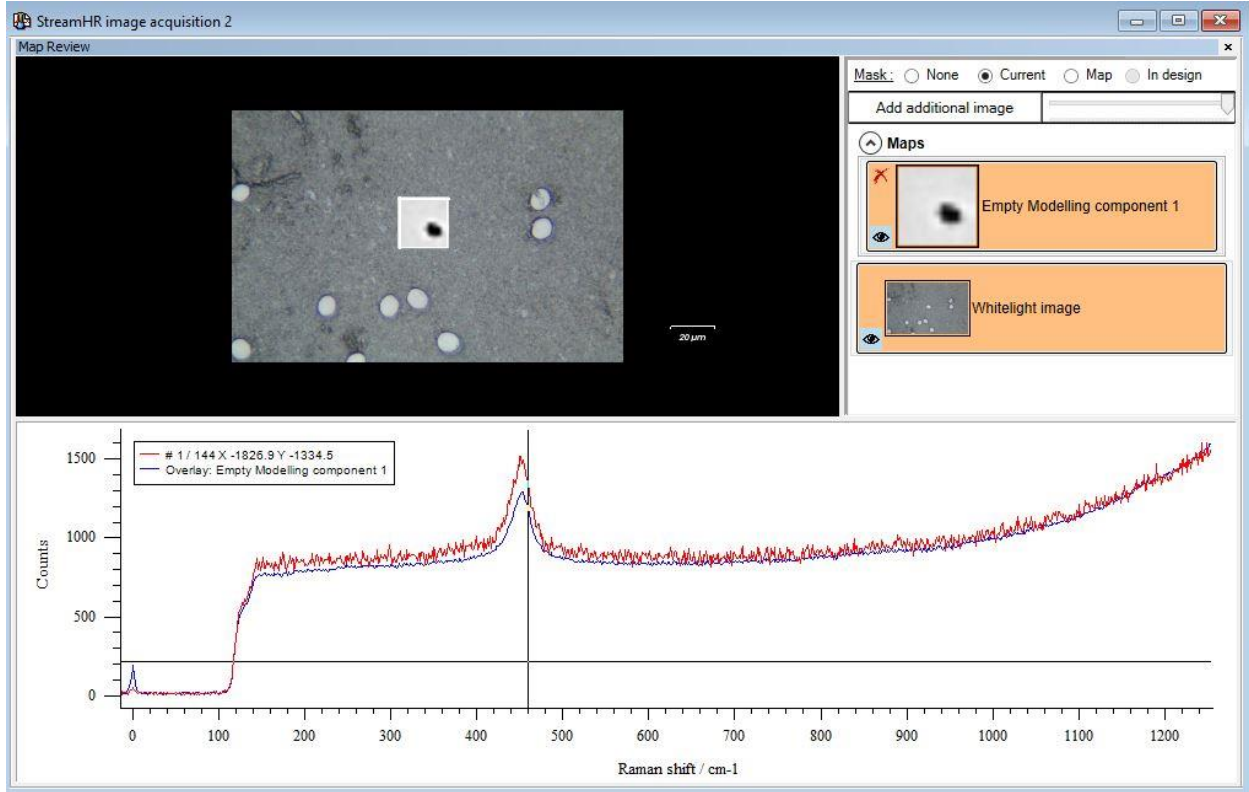


Figure 3.15. Raman map with empty modelling component 1 (blue) compared to a spectrum (red) for R3\_3.

Bright white spots were observed in the optical images of R4 samples. These did not correspond to  $\text{CeO}_2$ , but they were likely an artifact of carbon fibers. Overall, the distribution of  $\text{CeO}_2$  particles in the images is similar to that shown in R2 (compare to Figure 3.13). Additional maps could be acquired to determine whether the difference is statistically significant.



**Figure 3.16. Raman map with empty modelling component 1 (blue) compared to a spectrum (red) for R5\_S3.**  
Note dark region corresponding to carbon fiber.

### 3.3 OPTICAL IMAGES

Optical images of each sample were acquired (R1–5) with each PIP cycle. The sample fracture morphology can be observed in optical images and in the SEM images shown in Section 3.4. Examples images following the third PIP cycles are shown in Figure 3.16 through Figure 3.21. Images were collected with the 5×, 10×, 20×, 50×, and 100× objectives. Only the 20× images are shown for each sample here. Cracking, pores, voids, and particulates are evident on the surface of each sample. Samples from R2 and R5 appear to have the least amount of cracking; these samples also show the highest concentration of fiber. Samples without  $\text{SiC}_f$  or  $\text{C}_f$  appear to have the largest cracks (Figure 3.18 and Figure 3.19). This could be an inherent sample trait, or it may be a result of sample preparation methods. Carbon fiber regions were clearly identified as the circular bright spots which are approximately 8  $\mu\text{m}$  in diameter in sample R5 (see Figure 3.14 and Figure 3.15). The distribution of fibers in this sample is as expected.

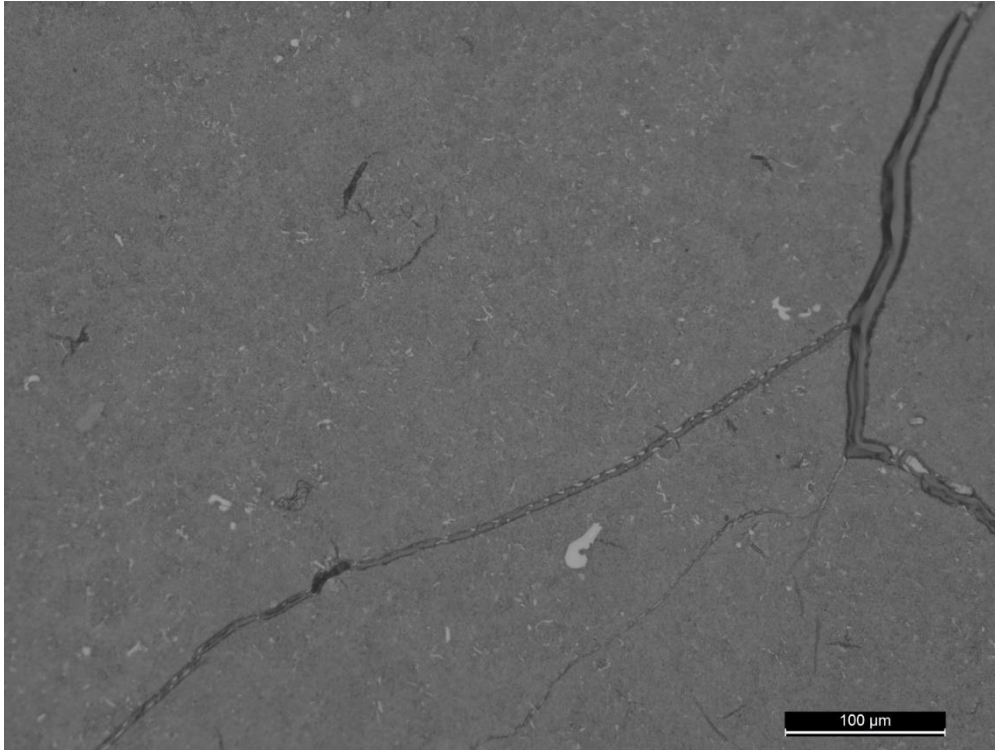


**Figure 3.17.** Optical image for sample R1\_3 using the 20× objective.

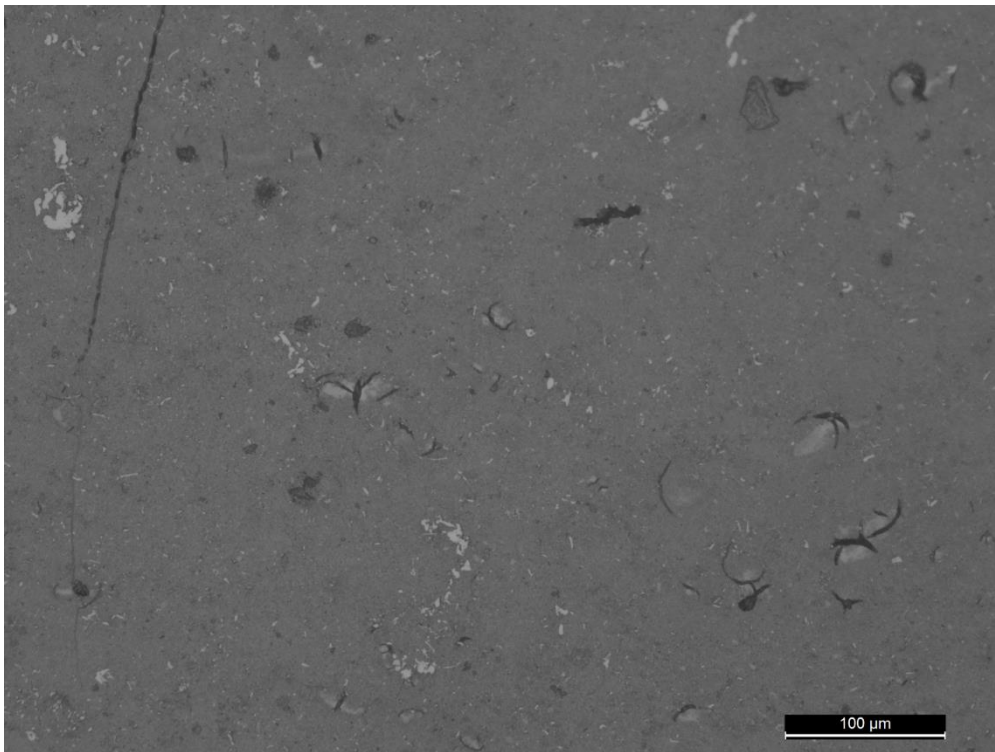


**Figure 3.18.** Optical image for sample R2\_3 using the 20× objective.

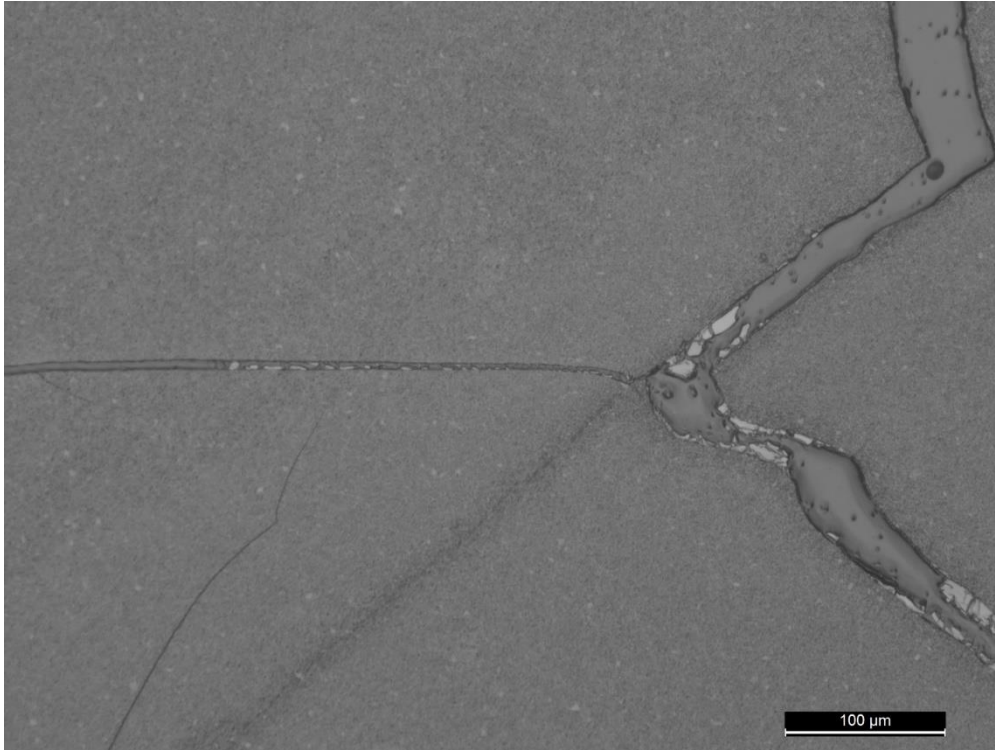


**Figure 3.19.** Optical image for sample R3\_3 using the 20× objective.

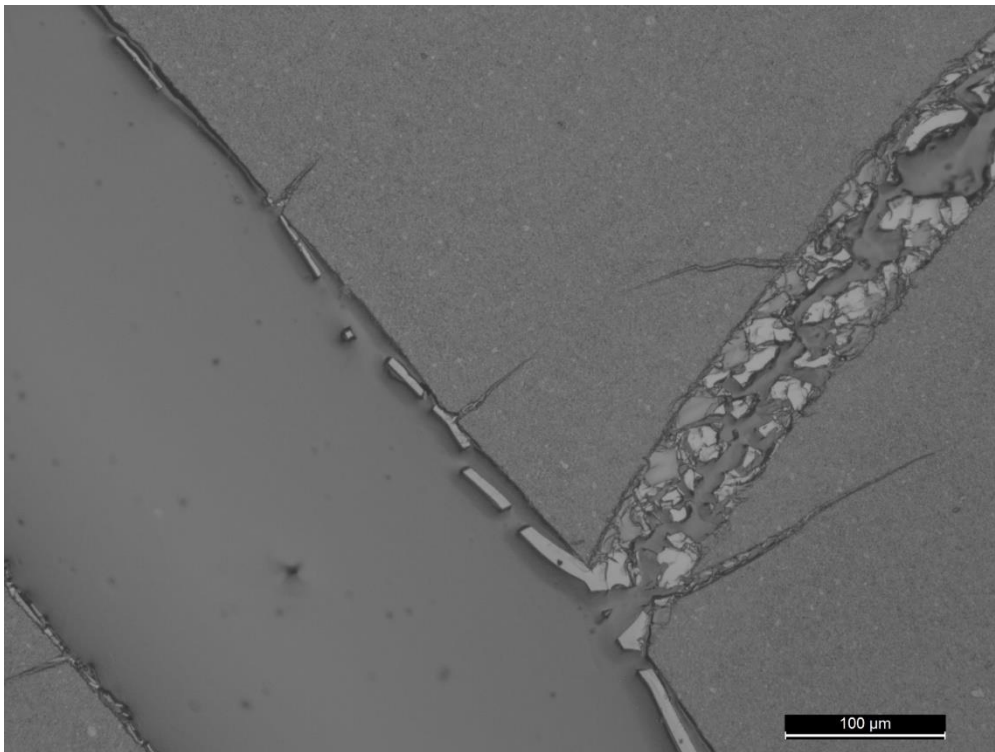


**Figure 3.20.** Optical image for sample R4\_3 using the 20× objective.

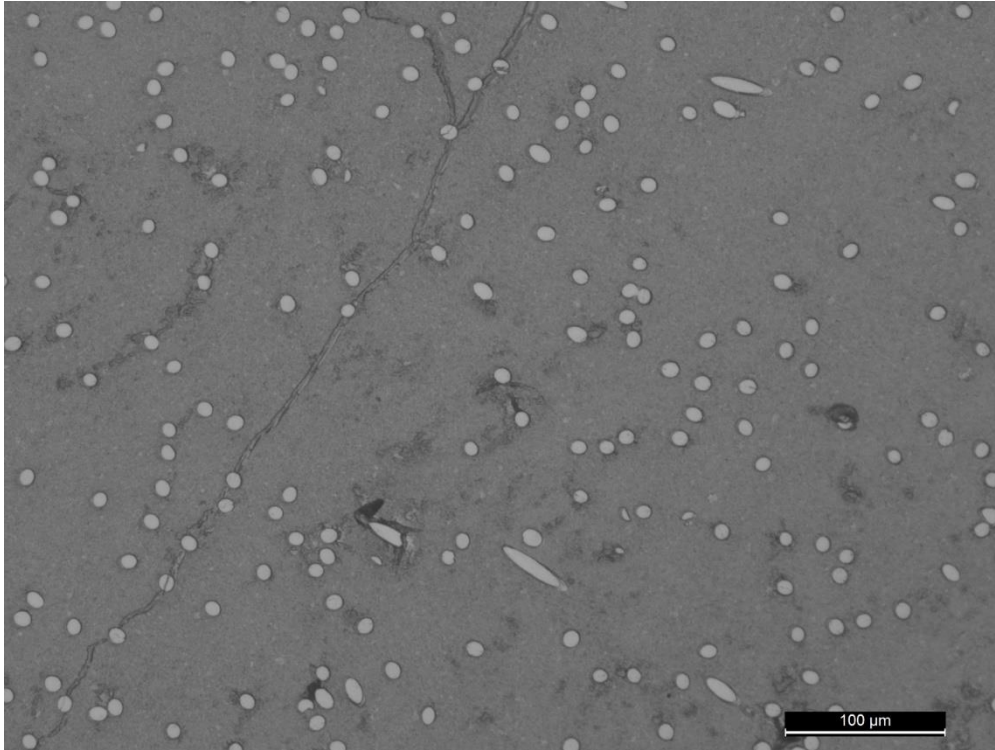


**Figure 3.21.** Optical image for sample R5\_3 using the 20× objective.

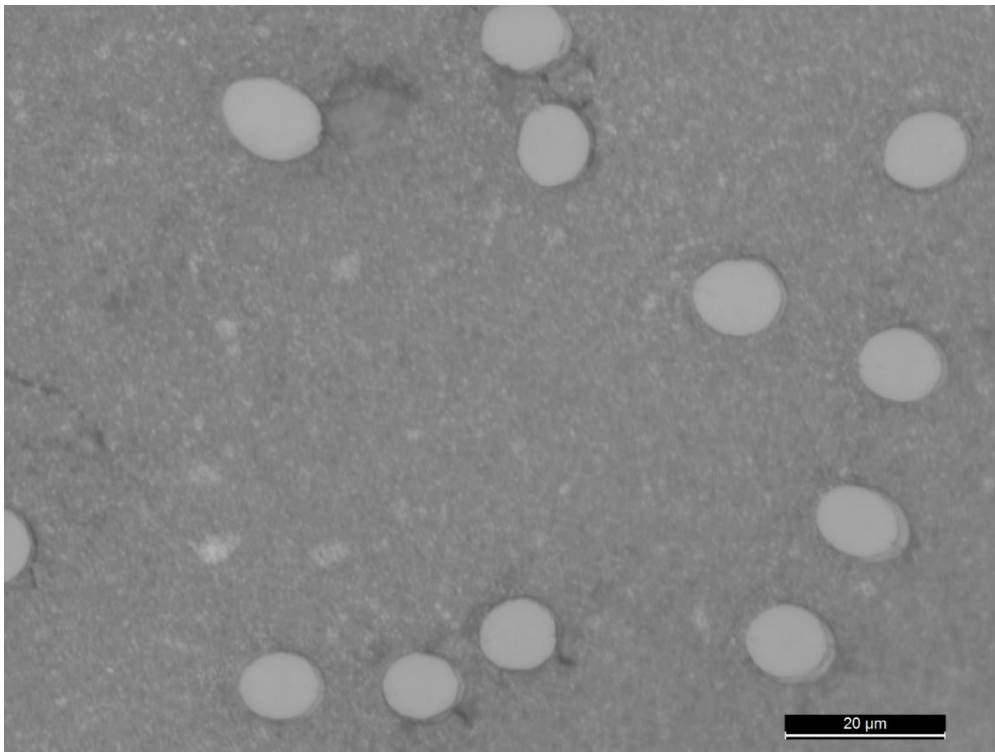


**Figure 3.22.** Optical image for sample R5\_3 using the 100× objective.

### 3.4 SEM-EDS ANALYSIS

#### 3.4.1 SEM and BSE Images

SEM was used to probe the morphological characteristics of the sample surfaces, and EDS was used to generate information about the chemical compositions of the samples. Imaging in backscatter electron (BSE) mode shows compositional differences based on the atomic number of each element present in the sample. High-Z material is associated with brighter white regions compared to darker regions made of low Z-material. The samples appeared to be relatively homogenous when imaged at low magnification (~200  $\mu\text{m}$  scale bar). However, increasing the magnification to 6,000 $\times$  (5  $\mu\text{m}$  scale bar) revealed the presence of small (<1  $\mu\text{m}$ ) Ce- and O-containing particles (Figure 3.22 through Figure 3.26). The images with fewer, less evenly distributed particles correspond to R1 and R3, which initially had less  $\text{CeO}_2$ . Imaging identified numerous regions where the particles were not agglomerated but were evenly distributed within the SiC matrix. This was particularly evident in the samples with higher concentrations of  $\text{CeO}_2$  relative to preceramic polymer. Although it appears that the particles are not bound or coated by the SiC fiber, this may simply be a result of etching. It is likely that the Ce-containing particles are fixed within the SiC composite.

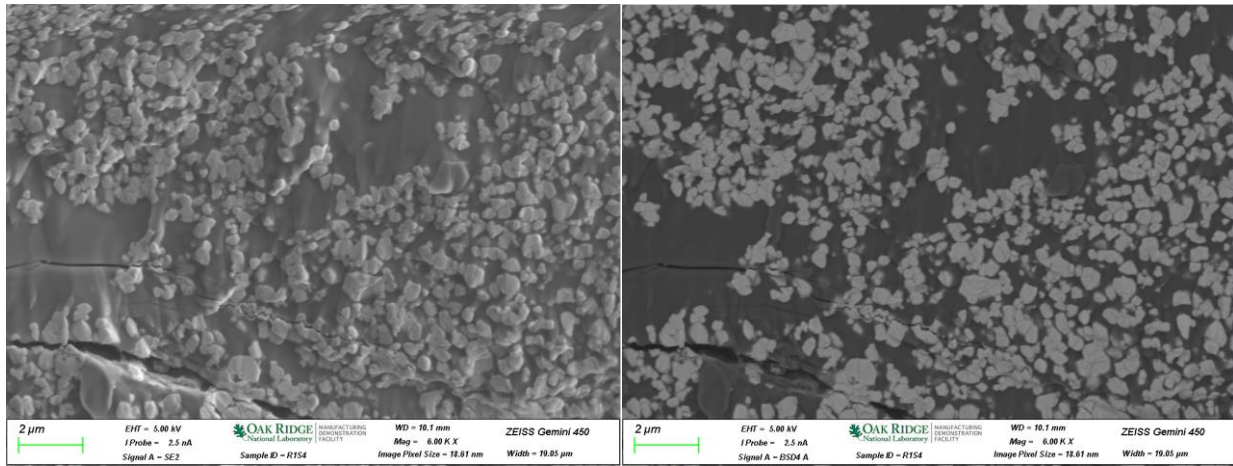


Figure 3.23. SEM image (left) in BSE mode (right) for R1. Bright particles (<1  $\mu\text{m}$ ) correspond to high-Z material (i.e., Ce oxides).

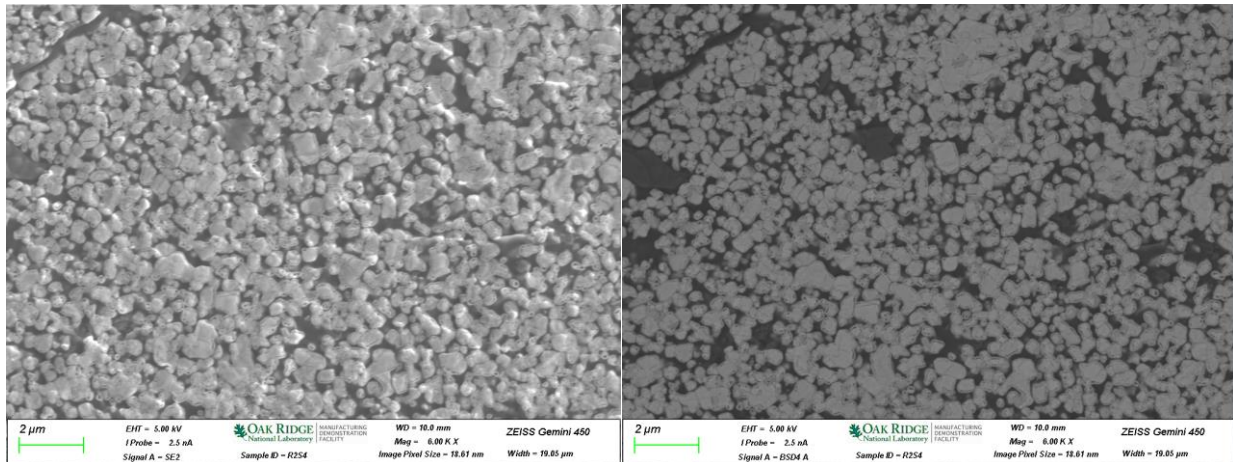
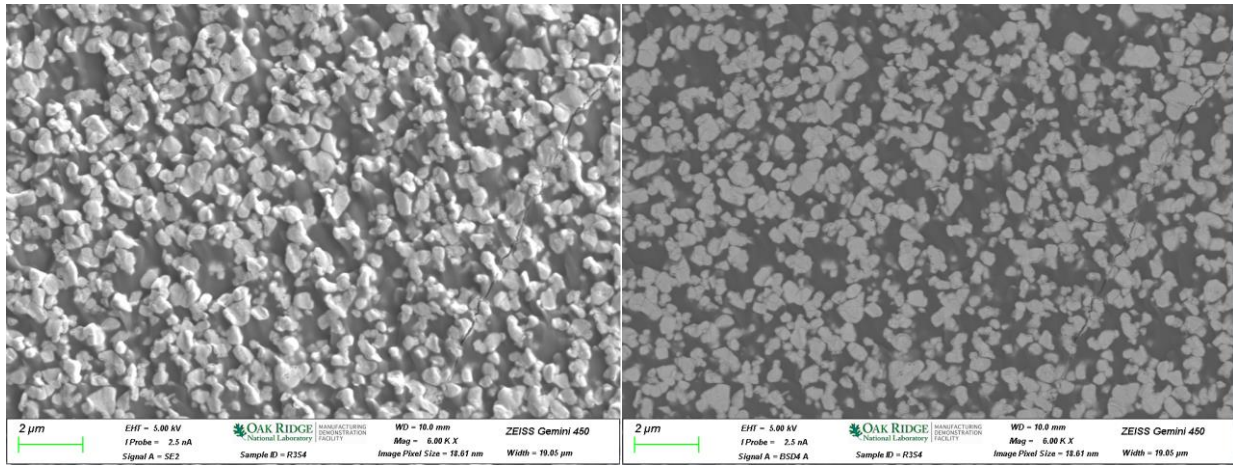
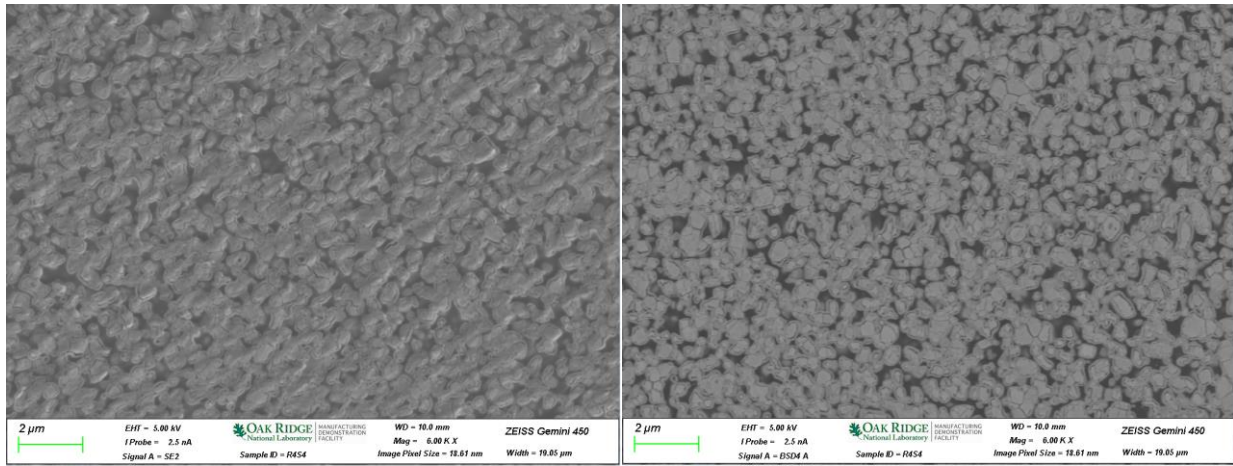


Figure 3.24. SEM image (left) in BSE mode (right) for R2. Bright particles (<1  $\mu\text{m}$ ) correspond to high-Z material (i.e., Ce oxides).



**Figure 3.25. SEM image (left) in BSE mode (right) for R3. Bright particles (<1 μm) correspond to high-Z material (i.e., Ce oxides).**



**Figure 3.26. SEM image (left) in BSE mode (right) for R4. Bright particles (<1 μm) correspond to high-Z material (i.e., Ce oxides).**

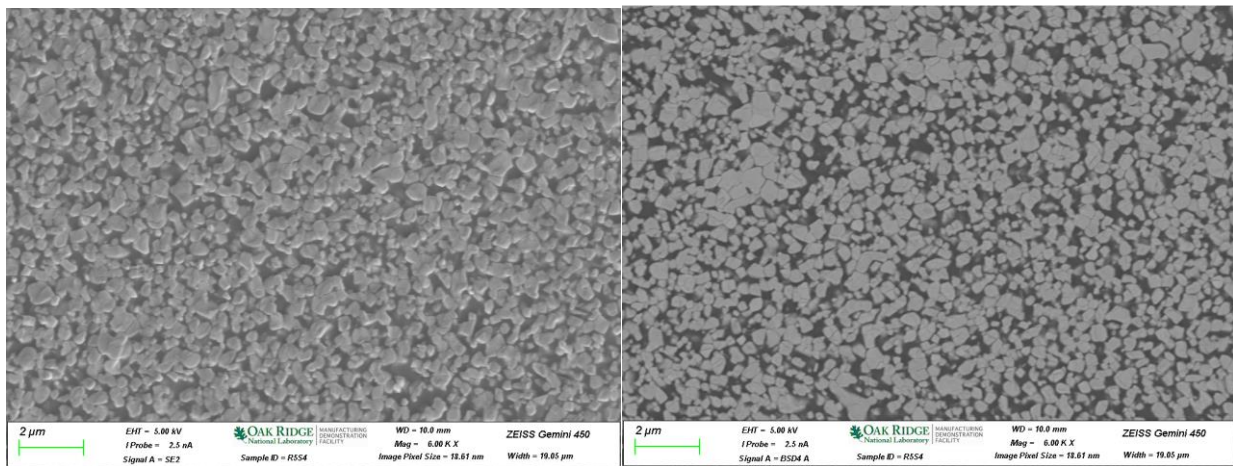


**Figure 3.27. SEM image (left) in BSE mode (right) for R5. Bright particles (<1 μm) correspond to high-Z material (i.e., Ce oxides).**

### 3.4.2 EDS Maps

To confirm elemental compositions for C, Si, Ce, and O, EDS maps were taken in various regions of the samples and at different levels of magnification (150–6,000×). Carbon (red), oxygen (green), Si (dark blue), and Ce (light blue) distributions were identified in each sample (Figure 3.27 through Figure 3.32). The bright particulates corresponded to Ce- and O-containing species and are likely Ce oxide(s). The elemental composition of the samples appears to be somewhat homogenous when data are acquired at low magnification (~ 200 μm scale bar), but it appears to be less homogenous at higher magnification (compare Figure 3.29 and Figure 3.30). The elemental distribution appears to be more homogenous at higher magnification in the samples with higher starting concentrations of CeO<sub>2</sub>.

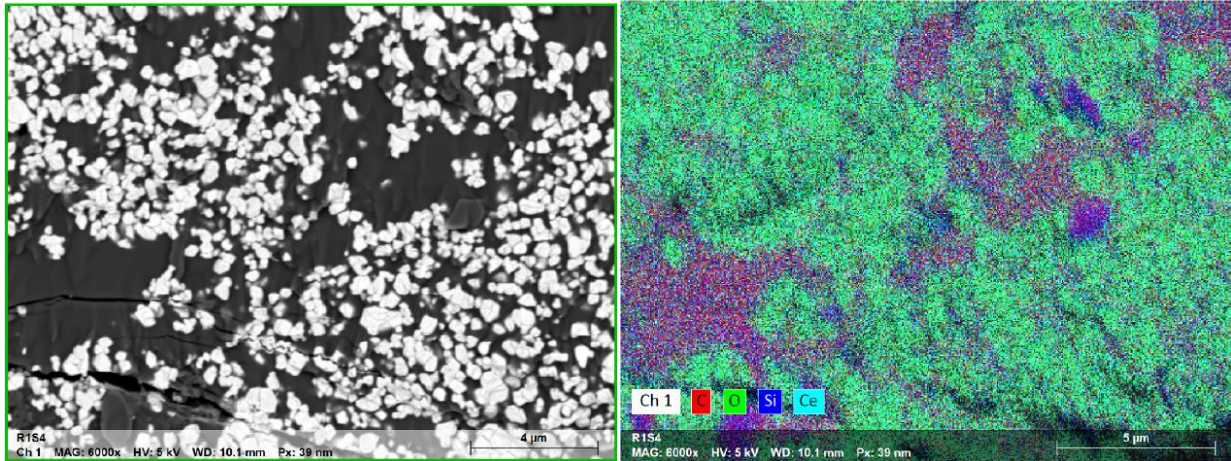


**Figure 3.28. SEM image (left) and BSE elemental map (right) for R1.** EDS results indicate that bright regions likely correspond to Ce oxide particles. Note the 5 μm scale bar.

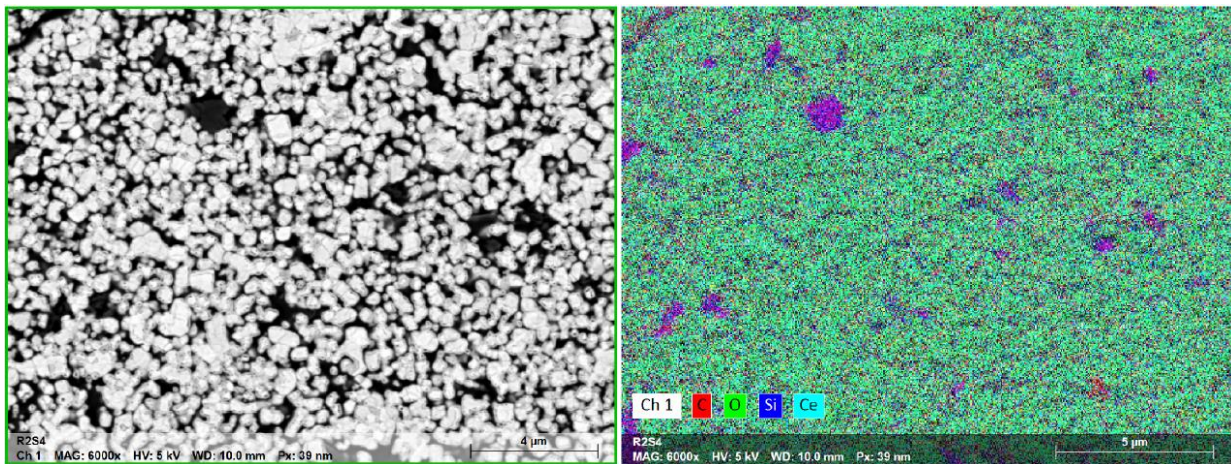


**Figure 3.29. SEM image (left) and BSE elemental map (right) for R2.** EDS results indicate that bright regions likely correspond to Ce oxide particles. Note the 5 μm scale bar.

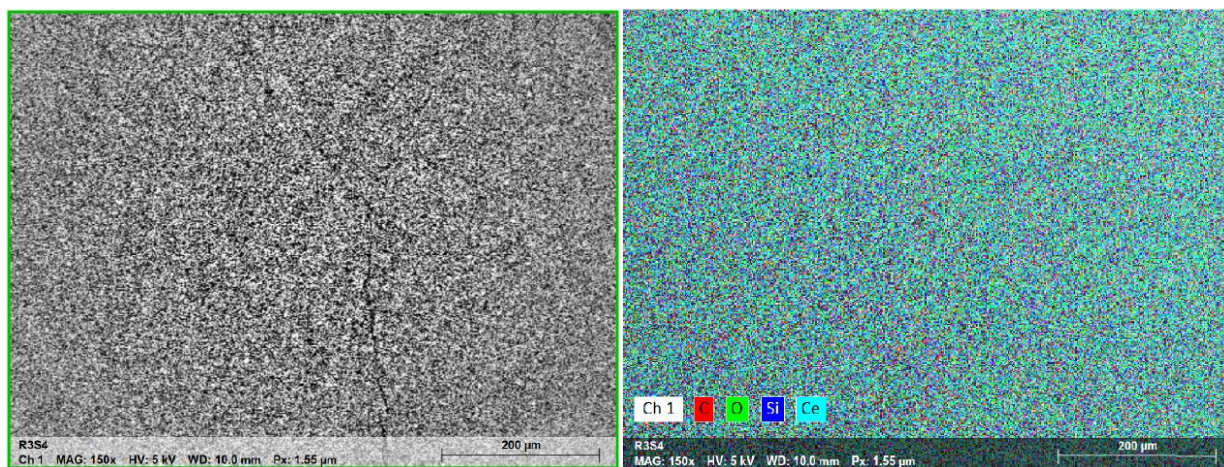


**Figure 3.30. SEM image (left) and BSE elemental map (right) for R3.** EDS results indicate that bright regions likely correspond to Ce oxide particles. Note the 200 µm scale bar.

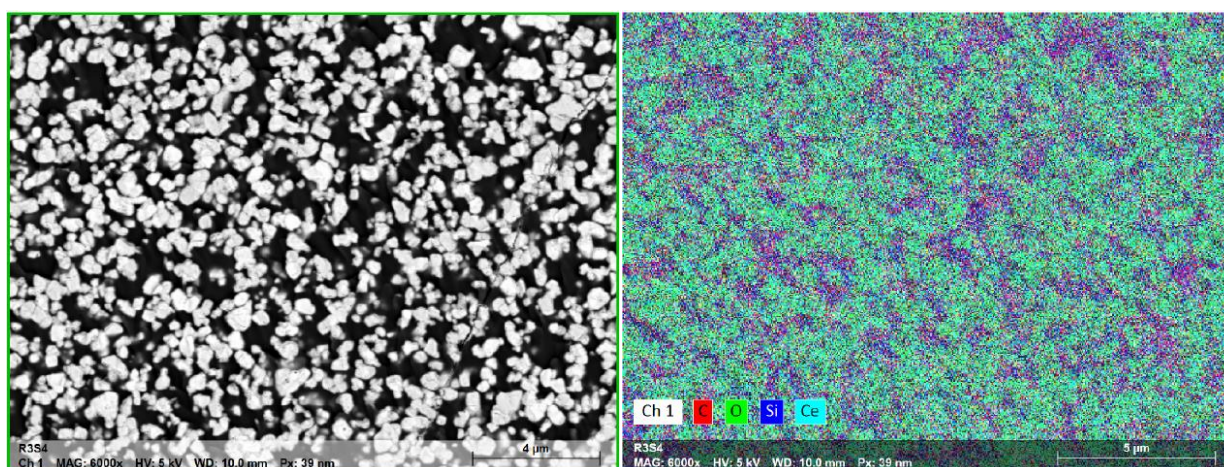


**Figure 3.31. SEM image (left) and BSE elemental map (right) for R3.** EDS results indicate that bright regions likely correspond to Ce oxide particles. Note the 5 µm scale bar.

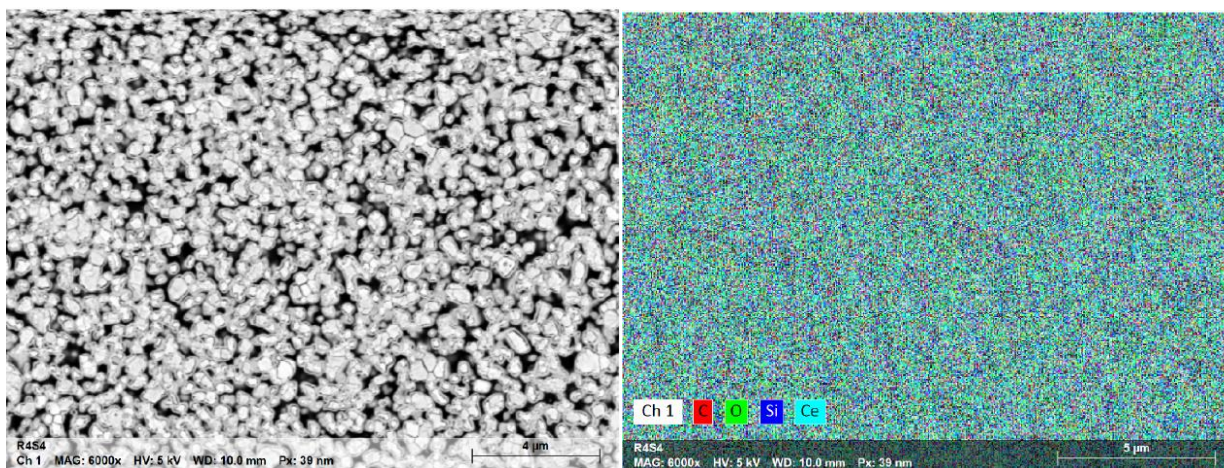


**Figure 3.32. SEM image (left) and BSE elemental map (right) for R4.** EDS results indicate that bright regions likely correspond to Ce oxide particles. Note the 5 µm scale bar.

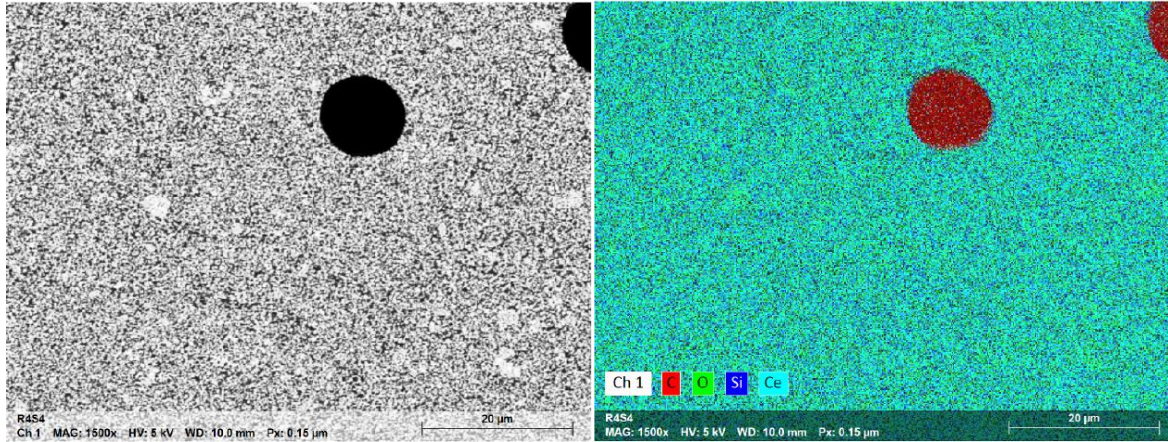


**Figure 3.33. SEM image (left) and BSE elemental map (right) for R5.** EDS results indicate that bright regions likely correspond to Ce oxide particles. Note the 20 µm scale bar.

### 3.5 DENSITY MEASUREMENTS

The initial synthesis of SiC parts from preceramic polymers results in porous composites that are typically 20–40 % in porosity. To reduce porosity below 7%, 6–9 PIP cycles are recommended. After the first several cycles, the composites can be cut to shape. Several PIP cycles were completed to minimize the porosity and to increase sample density (see Table 3.1). Part density did not increase substantially with addition PIP cycles. Samples with less CeO<sub>2</sub> (R1 and R3) were generally less dense than samples with more CeO<sub>2</sub> (R2, R4 and R5). Several samples were inconsistent with the others in the batch, possibly a result of the presence of nonclosed porosity (i.e., cracks) in the parts. To fully densify parts (<2% porosity), higher temperature heat treatments up to 1,000 °C, followed by PIP cycles to seal the porosity generated by the higher temperature, could be tested.

**Table 3.1. Sample density profiles**

Sample ID (Recipe no.)*	Sample mass (g)	Sample volume (cm <sup>3</sup> )	Sample density (g/cm <sup>3</sup> )	Standard deviation (STD) (g/cm <sup>3</sup> )
R1_1	1.9884	0.6363	3.1251	0.0012
R1_2	2.7483	0.7456	3.6861	0.0071
R1_3	3.6316	0.9835	3.6925	0.0044
R2_1	2.9564	0.6666	4.4349	0.0072
R2_2	2.8727	0.6410	4.4818	0.0022
R2_3	2.5596	0.5984	4.2776	0.0049
R3_1	2.3525	0.6537	3.5985	0.0029
R3_2	3.0326	0.8415	3.6039	0.0061
R3_3	3.1379	0.8923	3.5167	0.0055
R4_1	2.6974	0.6471	4.1685	0.0019
R4_2	3.6316	0.9835	3.6925	0.0044
R4_3	2.2326	0.5265	4.2406	0.0050
R5_1	3.2227	0.7585	4.2489	0.0016
R5_2	2.5473	0.6175	4.1249	0.0094
R5_3	2.9080	0.7181	4.0499	0.0052

\*R1–R5 refer to the five recipes listed in Table 2.1, and \_1, \_2, and \_3 refer to subsequent PIP cycles.

## 4. SUMMARY AND MAJOR CONCLUSIONS

### 4.1 FUTURE STUDIES AND APPLICATIONS

In the future, dissolution tests should be performed to determine how much of the  $\text{CeO}_2$  was captured within the SiC composite matrix and made chemically inert. This would determine whether the Ce could be recovered by traditional dissolution methods and if the  $\text{CeO}_2$  had been effectively sequestered by the composite. Studies could also be performed to examine different  $\text{CeO}_2/\text{SMP-10}/\text{SiC}_f/\text{C}_f$  ratios and various temperature ramp rates and holding durations. Cured ceramic polymer matrices are highly dependent on both temperature and time.<sup>4</sup> The work described here explored parameters near the highest possible oxide loading. Future work could explore additional oxide loading recipes with more  $\text{SiC}_f$  to improve fracture resistance and homogenous incorporation at the microscale.

Although microscale incorporation was debatable, this approach was certainly successful at incorporating  $\text{CeO}_2$  in a SiC matrix at the macroscopic level. After the synthesis of a part is completed following one of the recipes outlined here, it could be advantageous to place the part in a larger 3D printed mold and follow the same synthesis or SiC foam to form a SiC composite surrounding the initial part.<sup>6</sup> This would further sequester the  $\text{CeO}_2$  powder if an appropriate level of tensile strength and low porosity were achieved. In addition to developing a robust composite, it would be interesting to pursue a method to 3D print a scaffolding that would hold SiC parts in desirable orientations while testing various materials that are thermodynamically stable and chemically inert.

### 4.2 CONCLUSIONS

This work pioneered several proof-of-principle experiments demonstrating the possibility of capturing oxide powder within a SiC composite matrix. Parts with a higher loading of  $\text{CeO}_2$  and more  $\text{SiC}_f$  appeared to be more homogenous on the microscale and were less brittle. Tensile strength and hardness testing could be analyzed in future work on these samples to obtain more quantitative measures of relative properties. Raman maps were useful for measuring the distribution of  $\text{CeO}_2$  and other potential impurities within the matrix, and they revealed some regions where particles were agglomerated. The  $\text{CeO}_2$  Raman  $T_{2g}$  band peak intensity and FWHM properties provided more complementary information about the microscale distribution of Ce-containing species on the surface than EDS mapping could provide. Although there appeared to be regions of homogeneity in each sample, there were also nonhomogeneous regions with voids, chemical segregation, and pores. Future work could focus on testing a wider range of conditions (temperatures, cycles, etc.) with different amounts of  $\text{SiC}_f$  and  $\text{CeO}_2$  to improve composite properties.

## REFERENCES

- [1] Blue Ribbon Commission on America's Nuclear Future. *Disposal Subcommittee Report to the Full Commission: Updated Report*, US Government Printing Office: Washington, DC, 2012.
- [2] P. Sellin and O. X. Leupin. "The Use of Clay as an Engineered Barrier in Radioactive Management – A Review." *Clays Clay Miner.* 2013, 61 (6), 477–498.
- [3] L. L. Snead et al., "Handbook of SiC Properties for Fuel Performance Modeling." *J. Nuc. Mater.*, 2007, 371 ,329–377.
- [4] T. S. Key, D. K. Patel, G. B. Wilks, and M. K. Cinibulk, "Modeling the Pyrolysis of Pre ceramic Polymers: A Kinetic Study of the Polycarbosilane SMP-10." *J. Eur. Ceram. Soc.* 2021, 41, 6356–6365.
- [5] D. W. Wheeler and I. A. Khan, "Raman Spectroscopy Study of Cerium Oxide in a Cerium-5 wt.% Lanthanum Alloy." *Vib. Spectrosc.* 2014, 70, 200–206.
- [6] P. Jana, E. Zera, and G. D. Soraru, "Processing of Pre ceramic Polymer to Low Density Silicon Carbide Foam." *Mater. Des.* 2017, 116, 278–286.

